

Hubble Frontier Field Clusters and their Parallel Fields: Photometric and Photometric Redshift CatalogsA. PAGUL,¹ F. J. SÁNCHEZ,² I. DAVIDZON,³ AND BAHRAM MOBASHER¹¹*Department of Physics and Astronomy, University of California Riverside, Pierce Hall, Riverside, CA., USA*²*Fermi National Accelerator Laboratory, Wilson Hall, Batavia, IL., USA*³*The Cosmic Dawn Center, Vibenshuset, Lyngbyvej 2, Copenhagen, Denmark*

(Accepted February 26, 2021)

ABSTRACT

We present a multi-band analysis of the six *Hubble* Frontier Field clusters and their parallel fields, producing catalogs with measurements of source photometry and photometric redshifts^{a)}. We release these catalogs to the public along with maps of intracluster light and models for the brightest galaxies in each field. This rich data set covers a wavelength range from 0.2 to 8 μm , utilizing data from the *Hubble* Space Telescope, Keck Observatories, Very Large Telescope array, and *Spitzer* Space Telescope. We validate our products by injecting into our fields and recovering a population of synthetic objects with similar characteristics as in real extragalactic surveys. The photometric catalogs contain a total of over 32,000 entries with 50% completeness at a threshold of $\text{mag}_{\text{AB}} \sim 29.1$ for unblended sources, and $\text{mag}_{\text{AB}} \sim 29$ for blended ones, in the IR-Weighted detection band. Photometric redshifts were obtained by means of template fitting and have an average outlier fraction of 10.3% and scatter $\sigma = 0.067$ when compared to spectroscopic estimates. The software we devised, after being tested in the present work, will be applied to new data sets from ongoing and future surveys.

Keywords: HST photometry – Galaxy clusters – Intracluster medium

1. INTRODUCTION

To develop a comprehensive picture of the primordial building blocks of the universe, identification and study of properties of the youngest galaxies (< 1 Gyr) soon after the Big Bang is essential. Given their enormous distance, these systems are best detected at near-infrared wavelengths. However, because of high sky background at these wavelengths, such observations need to be done from space- i.e. using the *Hubble* Space Telescope (HST) or *James Webb* Space Telescope (JWST). This also requires multi-waveband observations spanning a range of wavelengths from optical and near-infrared. Furthermore, study of galaxies at these redshifts is often biased as we mainly sample the intrinsically brighter populations.

To accomplish the above, very deep multi-waveband observations over a large area are needed to detect statistically representative samples of very high redshift galaxies. This is currently beyond the reach of the largest available telescopes. To achieve such depths, one could leverage the natural phenomenon of gravitational lensing by targeting rich clusters of galaxies (Schneider 1984; Blandford & Narayan 1986, and ref-

erences thereon) (see Kneib & Natarajan 2011, for a review). This magnifies fluxes from high redshift sources located behind massive galaxy clusters, helping to probe deeper into the universe. This will be highly beneficial for even after the largest space telescopes (i.e. JWST), with their unprecedented sensitivity, are commissioned. It has been demonstrated that JWST will be able to shed light on the mechanisms that re-ionized the intergalactic medium at $6 < z < 10$ only by exploiting the cluster lensing phenomenon, to observe galaxies with $M < 10^9 M_{\odot}$ (Atek et al. 2018).

The *Hubble* Frontier Field program (HFF, Lotz et al. 2017) is a survey, designed with these objectives in mind. With an allocation of 630 HST orbits, it performed deep observations of six very massive clusters and their parallel fields in optical and near-IR bands, with Advanced Camera for Surveys (ACS) and Wide Field Camera 3 (WFC3), respectively. In addition, each field has been extensively observed in the mid-IR regime (between 3 and 5 μm) with the Infrared Array Camera (IRAC) on board the *Spitzer* Space Telescope.

The six clusters span the redshift range $0.3 < z < 0.55$ and their magnification power allows detection of galaxies up to $z \sim 9$, i.e. at the re-ionization epoch (see Barkana & Loeb 2001; Miralda-Escudé 2003). HFF followed the successful tradition of deep, pencil-beam HST

^{a)} Catalogs can be found [here](#).

observations as in *Hubble* Deep Field (Williams 1995), *Hubble* Ultra-Deep Field (HUDF, Beckwith et al. 2006) and CANDELS (Koekemoer et al. 2011), as well as programs covering wider areas like the Cosmic Evolution Survey (COSMOS, Scoville et al. 2007) and Galaxy Evolution from Morphology and SED (GEMS, Rix et al. 2004). With respect to galaxy cluster observations, the Cluster Lensing And Supernovae survey with *Hubble* (CLASH, Postman et al. 2012) paved the way for the HFF.

The HFF clusters will be the reference fields for the exploration of the distant universe. At present, additional HST coverage is provided by the “Beyond Ultra-deep Frontier Fields and Legacy Observations” (BUFFALO, Steinhardt et al. 2020) which aims at covering the outskirts of the HFF clusters over the same wavebands and to the same depth, as well as increasing the depth in the centers of the clusters. Most notably, sources in the HFF clusters will also be JWST targets, with some of them already selected by both Guaranteed Time Observation teams¹ and an Early Release Science Program². Eventually, the knowledge acquired from the HFF shall be applied to analyze data from an unprecedented number of galaxy clusters that *Euclid* and *Roman* space telescopes will discover by surveying thousands of square degrees of the sky (Laureijs et al. 2011; Spergel et al. 2015).

Apart from providing access to the high redshift Universe, the HFF will also allow the study of properties of dark matter (e.g. Jauzac et al. 2015, and references therein) and the role of ‘environment’ in the evolution of galaxies at $z < 1$ (e.g. Gao et al. 2005; Paranjape et al. 2018). It will also provide a standard sample of cluster galaxies, to be compared with nearby systems. The HFF parallel fields provide similar data to the same depth, that would minimize selection effects and biases in any environmental study of galaxy populations. The cornerstone of all these studies is a multi-waveband photometric catalog, containing self-consistent photometry for every detected source. Producing such a catalog is particularly challenging, given the depth of the imaging data, analysis of images in the crowded fields, the wide wavelength baseline (which imply substantial changes in the point spread function) required, and contamination from the intra-cluster light (ICL). The task has already been fulfilled by two distinct teams (AstroDeep³ and DeepSpace⁴) which released their respective HFF catalogs to the astronomical community (Castellano et al. 2016; Di Criscienzo et al. 2017; Shipley et al. 2018;

Bradač et al. 2019). Given the challenges mentioned above in identifying individual sources, in performing accurate photometric measurements for the HFF galaxies, and in simultaneously dealing with a multiple parameter space, it is important to apply completely independent techniques to generate catalogs for the same clusters. This allows a better understanding of the final data products, selection effects and the caveats in the data and the data processing pipelines. In particular, the different data reduction steps could introduce systematic effects in the final results, which need to be studied. Such problems and inaccuracies in source identification and photometry will also be reflected into selection of different populations of galaxies. For example, comparing two independent estimates of photometric redshifts can be instrumental to selecting the most robust galaxy candidates at $z > 8$ (McLeod et al. 2016). The existing catalogs produced from the above mentioned studies contain serious discrepancies in the photometry of the same galaxies. An independent analysis will help us study the origins of these differences.

In this study, we generate new galaxy catalogs for the six HFF clusters and their parallel fields. The results include photometric catalogs, photometric redshifts, Intra-Cluster Light (ICL) maps, and surface brightness models to remove the brightest galaxies from our images in order to detect fainter galaxies to deeper levels. The parallel fields provide ancillary deep-field data and will also serve as control samples. The main differences between the strategy here and the previous methods is that, we provide models of the intra-cluster light maps, as well as perform forward modelling of photometry to characterize biases and uncertainties in flux measurements. Moreover, the pipelines developed for this study will be applied to the new BUFFALO data (Pagul et al., in prep.) to extend the HFF catalogs to wider areas, providing self-consistent data for the HFF and BUFFALO galaxies.

The paper is organized as follows. In Section 2 we introduce the data sets. Section 3 presents a detailed study of the data reduction, followed by source extraction in Section 4. In Section 5, we study the completeness and photometric uncertainties in HFF clusters, as well as include comparisons between our results and previous works. In Section 6 we present the photometric redshifts for the HFF measurements. In Section 7, we discuss the lensing measurements. Section 8 presents information about the released data products. Section 9 summarizes our results.

Throughout this paper we assume standard cosmology with $\Omega_M = 0.23$, $\Omega_\Lambda = 0.76$ and $H_0 = 73$ Km/sec/Mpc. Magnitudes are in the AB system.

2. THE DATA

2.1. *HST* observations

The HFF observations are the deepest of galaxy clusters to date, and second only to the HUDF when also

¹ as listed at this [http URL](http://www.astrondeep.eu/).

² Treu et al., program 1324 “Through the Looking GLASS: A JWST Exploration of Galaxy Formation and Evolution from Cosmic Dawn to Present Day”.

³ <http://www.astrondeep.eu/frontier-fields/>

⁴ <http://cosmos.phy.tufts.edu/~danilo/HFF/Home.html>

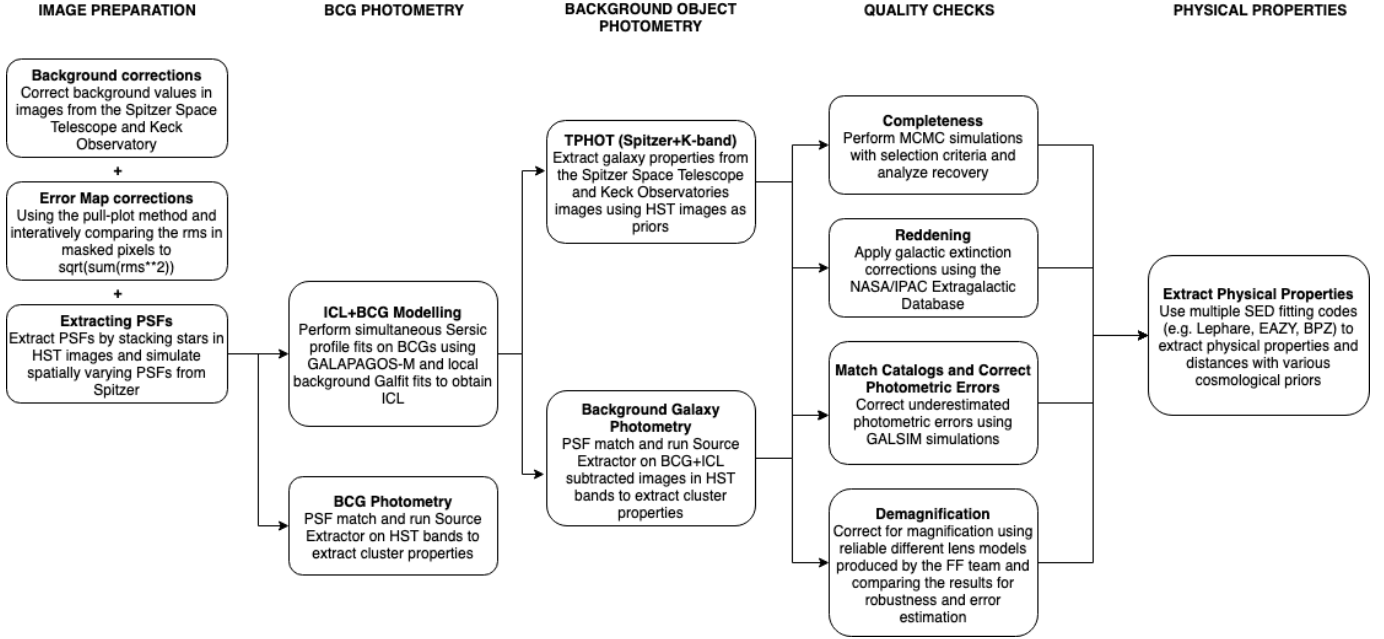


Figure 1. Workflow of the data processing as performed in the present work.

Table 1. Frontier Field cluster and parallel field positions, along with clusters’ mean redshift (z_{clu}), virial mass (M_{vir}), and X-ray luminosity (L_X) (Lotz et al. 2017)

Field	Cluster Center (J2000)	Parallel Center (J2000)	z_{clu}	M_{vir}	L_X
Abell 370	02:39:52.9, -01:34:36.5	02:40:13.4, -01:37:32.8	0.375	$\sim 1 \times 10^{15}$	1.1×10^{45}
MACS J0717.5+3745	07:17:34.0 +37:44:49.0	07:17:17.0 +37:49:47.3	0.545	$\sim 2 - 3 \times 10^{15}$	3.3×10^{45}
MACS J0416.1-2403	04:16:08.9, -24:04:28.7	04:16:33.1, -24:06:48.7	0.396	1.2×10^{15}	1.0×10^{45}
Abell S1063	22:48:44.4, -44:31:48.5	22:49:17.7, -44:32:43.8	0.348	1.4×10^{15}	1.8×10^{45}
Abell 2744	00:14:21.2, -30:23:50.1	00:13:53.6, -30:22:54.3	0.308	1.8×10^{15}	3.1×10^{45}
MACS J1149.5+2223	11:49:36.3, +22:23:58.1	11:49:40.5, +22:18:02.3	0.543	2.5×10^{15}	1.8×10^{45}

considering the blank fields. This results from a total of 840 orbits, performed through coordinated HST parallel observations in the following filters: F435W, F606W, F814W in ACS, and F105W, F125W, F140W, F160W in WFC3. These seven bands reached a depth of $m_{AB} \sim 29$ mag for point sources within a 0.4" diameter aperture (Lotz et al. 2017). Through a different program, UV observations in the F275W and F336W filters of two HFF clusters, Abell 2744 and MACS J0717, were carried out with details presented in (Alavi et al. 2016).

The gravitational potential of the clusters’ halo, besides binding together the galaxies in the system, produces a lensing magnification that could detect background objects to an *intrinsic* brightness of 30–33 mag, i.e. 10–100 times fainter than previous surveys. Details of the HFF survey design are provided in Lotz et al. (2017). In Table 1 we report the main characteristics of the six clusters, with a summary of the observations in Table 2. The filter throughput for the ACS and WFC3 instruments are shown in Figure 2 (upper panel). We use mosaics that have been reduced by the Frontier Fields

Table 2. The Point Spread Function and effective wavelengths for different photometric bands used for the HFF.

Band	$FWHM$	λ_{pivot} (Å)
F275W	0.075"	2707
F336W	0.109"	3355
F435W	0.109"	4329
F606W	0.112"	5922
F814W	0.111"	8045
F105W	0.175"	10551
F125W	0.176"	12486
F140W	0.172"	13923
F160W	0.173"	15369
Ks	0.364"	21524
I1	1.29"	35634
I2	1.42"	45110
I3	1.50"	57593
I4	1.84"	79595

NOTE—Representative PSF FWHM values for the photometric bands in this study. These values were calculated for the Abell 2744 cluster. Bands F275W and F336W are only available for Abell 2744 and MACS J0717. IRAC Channels 3 and 4 are only available for Abell 2744, Abell 370, Abell S1063, and MACS J0717.

team⁵, with a pixel scale of 0.06"/pix. These images have been reduced using the HST science data products pipeline (Koekemoer et al. 2011). Data from other HST programs using the same filters have also been included by the HFF team, with all the exposures aligned relative to each other using *Tweakreg*⁶. Other steps in the reduction process include: correction of standard imaging artifacts; bad pixel and cosmic ray rejection; geometric distortion correction and image stacking using *AstroDrizzle* (Gonzaga & et al. 2012). Throughout this work we will focus on the analysis and detection of these previously reduced and calibrated data.

2.2. Ancillary data

A number of independent observations of the HFF have generated complementary data to that available from the HST. The *Spitzer* Space Telescope dedicated

more than 1,000 hours of Director’s Discretionary time to obtain IRAC 3.6 μm (channel 1) and 4.6 μm (channel 2) imaging down to the depths of 26.5 and 26.0 mag., in cluster and parallel fields respectively. These observations are crucial for photometric redshift measurement, for identifying low-redshift interlopers, and are beneficial in constraining galaxy properties since they provide a good proxy for galaxy stellar mass. In addition, there are legacy IRAC observations at 5.8 μm (channel 3) and 8.0 μm (channel 4) which are also included in our analysis⁷. To produce the Frontier Fields mosaics, the following *Spitzer* Program IDs were used:

- Abell 2744: 83, 90275
- MACS J0416.1-2403: 80168, 90258
- MACS J0717.4+3745: 40652, 60034, 90009, 90259
- MACS J1149.4+2223: 60034, 90009, 90260
- Abell S1063 (RXC J2248.7-4431): 83, 10170, 60034
- Abell 370: 137, 10171, 60034

Another follow-up program is the K_s -band Imaging of the Frontier Fields (KIFF Brammer et al. 2016), carried out with the High Acuity Wide Field K-band Imager (HAWK-I) at the Very Large Telescope (VLT). This reached a depth of 26.0 mag (5σ , point-like sources) for Abell 2744, MACS-0416, Abell S1063, and Abell 370 clusters in the southern hemisphere. The K-band imaging campaign of the HFF also used the Multi-Object Spectrometer for Infrared Exploration (MOSFIRE) at Keck to observe MACS-0717 and MACS-1149 in the northern hemisphere to a 5σ depth of 25.5 and 25.1 mag respectively.

Table 3 provides a summary of the available ancillary data, with their filter transmission curves shown in Figure 2 (lower panel).

3. DATA REDUCTION

The workflow followed for the data processing in this work is presented in Figure 1.

3.1. Modeling the point spread function in different bands

Accurate knowledge of the point spread function (PSF) as a function of wavelength and optical system is crucial to perform consistent photometry within a ‘panchromatic’ baseline. Knowledge of the PSF for HFF galaxies is needed to reconstruct their intrinsic morphology as well as mapping the ICL (Section 3.2). To perform consistent multi-waveband photometry, taking

⁵ <https://archive.stsci.edu/prepds/frontier/>

⁶ part of the DrizzlePac software suite: <https://www.stsci.edu/scientific-community/software/drizzlepac.html>.

⁷ retrieved from the Spitzer Heritage Archive <https://sha.ipac.caltech.edu/applications/Spitzer/SHA/>

Table 3. Existing multi-wavelength HFF coverage from follow-up programs, as used in the present work. The $5\text{-}\sigma$ point-source depth was estimated by integrating the noise in a Gaussian PSF aperture with the values of FWHM given in Table 2.

Field	Observatory	Wavelengths	Depth	Reference
Abell 370	VLT/HAWK-I	$2.2\mu\text{m}$	~ 26.18	Brammer et al. (2016)
	<i>Spitzer</i> IRAC 1,2	$3.6\mu\text{m}, 4.5\mu\text{m}$	$\sim 25.19, 25.09$	(PI: T. Soifer and P. Capak)
	<i>Spitzer</i> IRAC 3,4 (cluster-only)	$5.8\mu\text{m}, 8.0\mu\text{m}$	$\sim 23.94, 23.39$	See Section 2.2
MACS J0717.5+3745	Keck/MOSFIRE	$2.2\mu\text{m}$	~ 25.31	Brammer et al. (2016)
	<i>Spitzer</i> IRAC 1,2,3,4	$3.5\mu\text{m}, 4.5\mu\text{m}$	$\sim 25.04, 25.17$	(PI: T. Soifer and P. Capak)
	<i>Spitzer</i> IRAC 3,4	$5.8\mu\text{m}, 8.0\mu\text{m}$	$\sim 23.94, 23.39$	See Section 2.2
MACS J0416.1-2403	VLT/HAWK-I	$2.2\mu\text{m}$	~ 26.25	Brammer et al. (2016)
	<i>Spitzer</i>	$3.5\mu\text{m}, 4.5\mu\text{m}$	$\sim 25.31, 25.44$	(PI: T. Soifer and P. Capak)
Abell S1063	VLT/HAWK-I	$2.2\mu\text{m}$	~ 26.31	Brammer et al. (2016)
	<i>Spitzer</i> IRAC 1,2	$3.6\mu\text{m}, 4.5\mu\text{m}$	$\sim 25.04, 25.04$	(PI: T. Soifer and P. Capak)
	<i>Spitzer</i> IRAC 3,4 (cluster-only)	$5.8\mu\text{m}, 8.0\mu\text{m}$	$\sim 22.96, 22.64$	See Section 2.2
Abell 2744	VLT/HAWK-I	$2.2\mu\text{m}$	~ 26.28	Brammer et al. (2016)
	<i>Spitzer</i> IRAC 1,2	$3.6\mu\text{m}, 4.5\mu\text{m}$	$\sim 25.32, 25.08$	(PI: T. Soifer and P. Capak)
	<i>Spitzer</i> IRAC 3,4 (cluster-only)	$5.8\mu\text{m}, 8.0\mu\text{m}$	$\sim 22.78, 22.45$	See Section 2.2
MACS J1149.5+2223	Keck/MOSFIRE	$2.2\mu\text{m}$	~ 25.41	Brammer et al. (2016)
	<i>Spitzer</i>	$3.5\mu\text{m}, 4.5\mu\text{m}$	$\sim 25.24, 25.01$	(PI: T. Soifer and P. Capak)

into account band-to-band variations, we need to convolve images to the same PSF. This task, known as ‘‘PSF matching’’, is performed via kernel convolution. Images in multi-wavelength surveys are often affected by different diffraction levels, which make it difficult to obtain homogeneous measurements e.g. of aperture photometry. Figure 3 illustrates the broad range of PSF sizes by showing postage stamps extracted from a few HFF images from ~ 0.3 to $3.6\mu\text{m}$. Besides the optical performance of the instrument itself, the final PSF model also depends on the specific observing strategy of the survey (depth, dithering, etc.) and in the case of ground-based facilities also on the seeing conditions (in the case of Figure 3, VLT/HAWK-I).

For HST data (divided between cluster vs. parallel fields), PSFs were estimated by stacking unsaturated stars. We use IRAF to visually inspect stellar light curves and determine whether an object is saturated. Then we stack unsaturated stars using the IDL routine **Star Finder** (Diolaiti et al. 2000). The resulting PSF models used in PSF-matching are $2.34'' \times 2.34''$ postage stamps in the HST and Ks bands, and $28.56''$ for *Spitzer*. These

sizes are chosen in order to enclose diffraction spikes (as one can see in Figure 3).

Our procedure works well for the HST images and the K_s band as the variation of the PSF across the image is small. However, stacking unsaturated stars does not produce a robust result in the mid-IR *Spitzer* channels. This is due to large variations of the PSF as a function of the position on the image as well as the asymmetry of its shape⁸. This makes IRAC PSFs depend on the orientation of the camera. Moreover, IRAC Channels 1 and 2 pixels undersample the response of a point source⁹. Thus, instead of **Star Finder**, we use a synthetic pixel response functions (PRF) that combines the information on the PSF, the detector sampling, and the intrapixel sensitivity variation in response to a point-like source. A PRF model for a given position on the IRAC mosaic is generated by the code PRFMap (A. Faisst, private communication) by taking into account the single-epoch frames contributing to that mosaic. To

⁸ See the *Spitzer*/IRAC handbook

⁹ More information in the the *Spitzer*/IRAC handbook.

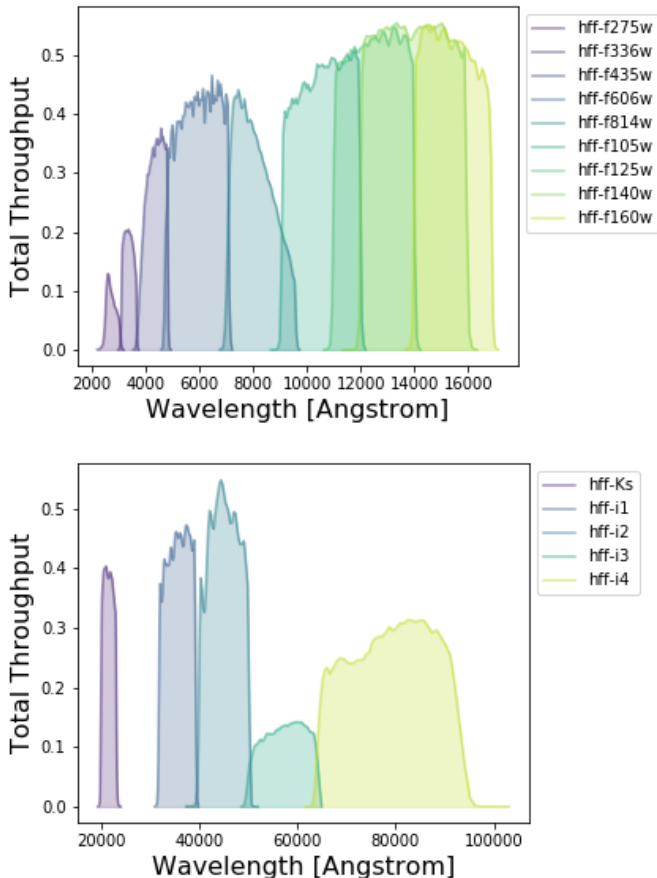


Figure 2. Throughput of the nine HST filters (*upper panel*) and ancillary Ks-band and IRAC bands (*lower panel*) used in this analysis.

do so, PRFMap stacks individual PRF models with the same orientation of the frames, resulting in a realistic, spatially-dependent PSF model (an example for IRAC channel 1 is shown in Figure 3).

We use GalSim in order to calculate the FWHM for each PSF/PRF listed in Table 2. More specifically, we use the `calculateFWHM` function, which computes the maximum intensity of the PSF, I_0 , the centroid of the PSF intensity, the first pixel from the centroid at which the intensity is $I < I_0/2$ and the last pixel at which the intensity is $I > I_0/2$, and then linearly interpolates between these two to estimate the value of the FWHM. For the Spitzer bands, we input into this function an averaged stack of all the normalized PRFs modelled in the field for a more conservative estimate.

3.2. Modeling the intra-cluster light

Given the richness of HFF clusters, those fields are particularly crowded with a significant probability of having cluster members aligned along the same line of sight of more distant background galaxies. The analysis of background systems is also impaired by the ICL,

i.e. the residual emission from stars that are generally not bound to any cluster galaxy (Montes & Trujillo 2019; Morishita et al. 2017; Sampaio-Santos et al. 2020). Blending between ICL and bright cluster galaxies is also a source of uncertainty. In an effort to alleviate these effects we attempt to model ICL and cluster members using GALFIT (Peng et al. 2010) and GALAPAGOS-2 (Barden et al. 2012; Häußler et al. 2013) respectively, following a similar procedure as in Morishita et al. (2017). Because the severity of the ICL-galaxy blending decreases towards the bluer wavelengths, we perform these fits for all but the bluest HST bands used here (i.e., *F275W* and *F336W*).

In this Section we focus on ICL modeling, while in Section 3.3 we will describe the procedure to fit the brightest cluster members. Subtracting their flux from the images will allow us to detect some of the faintest objects that otherwise would remain hidden by their overshining neighbors (see discussion in Section 4).

To model the ICL we follow the methodology presented in Morishita et al. (2017). We first run `Source Extractor` (Bertin & Arnouts 1996, hereafter SE) on each image/band to get a first-pass estimate of the morphological parameters of detected galaxies, and their segmentation map. In this way we can create a mask removing the detected pixels of sources fainter than 26 mag, as the fitting procedure (described below) is less reliable below that threshold. Then we produce a 18×18 arcsecond (300×300 pixel) patch for every remaining source, with the patch centered at the coordinate identified by SE as the centroid of the galaxy. By means of GALFIT, we simultaneously fit single Sérsic profiles to all the objects included in that patch. For patches whose GALFIT fits failed in the first instance, we randomly move the cutout center, creating five additional 18×18 arcsecond patches on which we run the same algorithm.

It should be noted that the number of patches across the field depends on the projected density of sources. This is illustrated in Figure 4 (left panel) by showing a representative “coverage map” for Abell 2744. In case a given pixel with coordinates (x, y) is only included in one cutout, the ICL emission (F_{ICL}) is defined as the local background measurement found by GALFIT (namely, the `sky value` parameter). If there are overlapping cutouts in (x, y) , we use the inverse χ^2 -weighted mean of their background measurements:

$$F_{ICL}(x, y) = \frac{\sum_i s_i(x, y) / \chi_i^2(x, y)}{\sum_i 1 / \chi_i^2(x, y)}, \quad (1)$$

where s_i and χ_i^2 are the `sky fit` and χ^2 values from GALFIT for the i -th cutout. The overall ICL map, in the case of Abell 2744, is shown in Figure 4 (middle panel).

The merged ICL map, represented by $F_{ICL}(x, y)$, may still contain some sharp features due to the finite nature of the cutouts used to build it. In order to avoid these

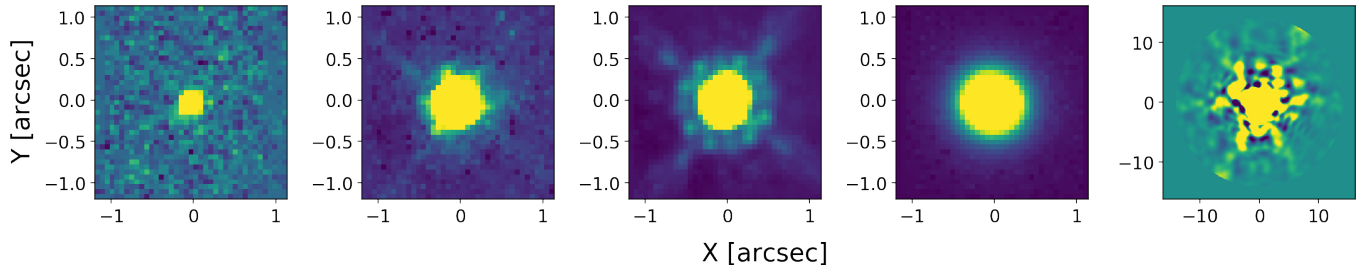


Figure 3. Representative examples of PSF for the instruments used in this study, corresponding to a $0.06''$ /pixel scale normalized with the `ZScale` algorithm. From left to right, panels show F336W (WFC3), F606W (ACS), F125W (WFC3), K_s (VLT), IRAC Channel 1 (*Spitzer*). See Section 3.1 for more details

features we introduce an additional step to the method presented in Morishita et al. (2017) by smoothing the merged ICL map with a Gaussian kernel. The size of this kernel is chosen by analyzing the (radially averaged) power spectrum of the coverage map (see the left panel of Figure 4) defined as $P(k) = \sum_{x,y} I_{r(x,y)} e^{-ikr}$, where r is the radial distance from the center of the image, $r = \sqrt{(x - x_0)^2 + (y - y_0)^2}$; x, y are the coordinates of each pixel, $I_{r(x,y)}$ is the value of the coverage map at the pixel x, y at a distance r from the center, and x_0, y_0 are the coordinates of the center of the image. We find this scale to be at $k \simeq 0.08$, i.e. about 72 pixels, or 4.32 arcseconds. In the right panel of Figure 4 we can see that this strategy successfully mitigates the impact of sharp features in the merged ICL map. As a sanity check, we generate a histogram of the sky background by masking sources using the corresponding segmentation map. We then compare this between the original image and the ICL subtracted image. We find that the resulting histogram of background pixels is both more symmetric, narrower, and centered at zero in the ICL subtracted image (Figure 5).

The resulting map, shown in Figure 4 for the Abell 2744 cluster, not only serves as a representative model of the ICL, but also as a background correction for the entire HFF mosaic. Figure 4 also shows the difference between the original map (middle image) and the one after kernel filtering (right-most image): The sharp flux gradients caused by finite box numbers and sizes is mitigated.

To model the ICL in the K_s and *Spitzer* images we use a local background routine built into the T-PHOT software (Merlin et al. 2016a), which calculates a background template for each object and merges them into a single image. As done in the optical and other near-infrared bands, we smooth the image with a representative kernel and subtract the result from the HFF mosaic. The smoothed ICL mosaics will be released as two-dimensional arrays in the same units (ADU/s) as the HFF mosaics.

3.3. Removal of the Bright Galaxies in Clusters

After correcting the cluster images for ICL and sky background, we model the brightest galaxy members of

each cluster (i.e. galaxies with $\text{MAGAUTO}_{\text{F160W}} < 19$). These objects are selected via a first-pass `SExtractor` run in the F160W band. The aim is to remove them and their diffuse light so that one could push the observations deeper. We use the publicly available code `GALAPAGOS-M`¹⁰ (Barden et al. 2012; Häußler et al. 2013), which is a software that automates source detection and bulge-disk Sérsic modeling, and takes advantage of multi-wavelength information in its parameter fits.

The advantage of using `GALAPAGOS-M` is in its ability to perform single and multi-component (bulge/disk decomposition) fits and to input galaxies using information from multiple bands *simultaneously*. In order to robustly measure color gradients in large galaxies, we restrict the degrees of freedom in the `GALAPAGOS-M` fits by imposing a wavelength dependency (with a quadratic function) for the half-light radius and Sérsic index. Compared to fitting morphology independently in each band, this approach is more stable and tightens the constraints of the morphological parameters measured for each galaxy (see Häußler et al. 2013). However, a multi-component model is susceptible to overfitting the images; therefore, we use the residual flux fraction (RFF, as in Hoyos et al. 2012) to assess the number of components that most effectively models the light profile of bright cluster members; such residual flux is obtained by subtracting the model from the input image. The residual flux fraction is a measure of signal excess in the residual image, not due to background fluctuations, and is defined as

$$\text{RFF} = \frac{\sum |I_{x,y} - I_{x,y}^{\text{model}}| - 0.8 \times \sum \sigma_{\text{BKG},x,y}}{\sum I_{x,y}}, \quad (2)$$

where $I_{x,y}$ and $I_{x,y}^{\text{model}}$ are respectively the observed and model fluxes for a given pixel with coordinates (x, y) , while $\sigma_{\text{BKG},x,y}$ is the background RMS in the same location. We sum over the pixels associated to a given galaxy. The 0.8 factor is included to ensure that the mean RFF of an image is null when it is exclusively affected by Gaussian noise with constant variance. For a given object to fit, we favor either a single- or two-

¹⁰ <https://github.com/MegaMorph/galapagos>

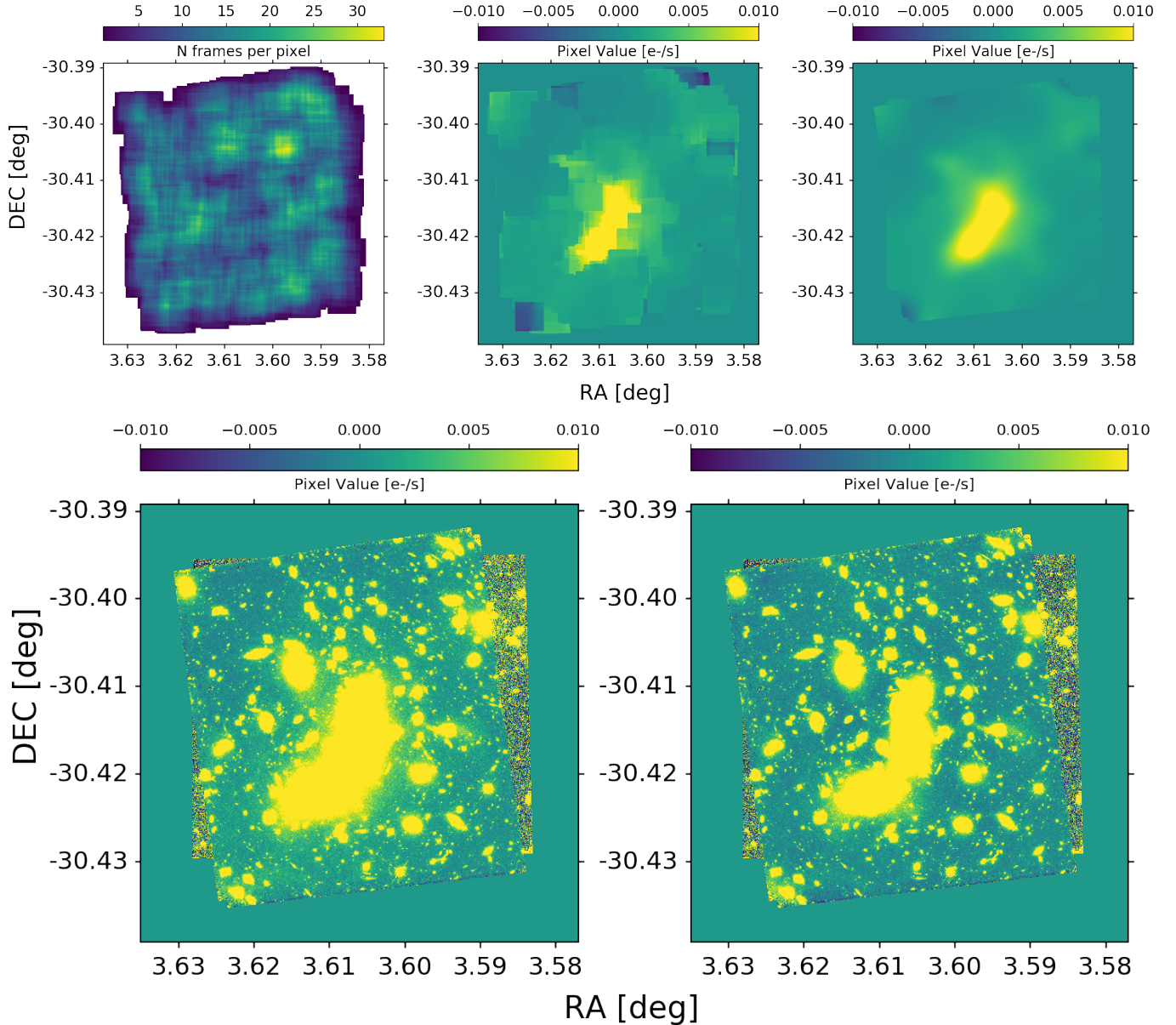


Figure 4. We illustrate the steps to generate the ICL map (as described in Section 3.2). Here the example is presented for the F160 band in Abell 2744. **Top Row:** *Left panel:* the “coverage map” showing the number of fit cutouts that overlap with each pixel. *Middle panel:* the resulting ICL map for the same band and cluster created by combining the fit background value of each cutout. Overlapping stamps are stacked using Eq. 1. *Right panel:* Final ICL map after smoothing the map in the Middle panel with a representative Gaussian kernel. More details about kernel creation as provided in section 3.2. **Bottom Row:** *Left panel:* Original Abell 2744 F160W science image. *Right panel:* F160W image after smoothed ICL (top row, right panel) subtraction.

component model depending on which of them results in the smallest RFF. Generally, studies of galaxy morphology require the RFF relative difference between two models, i.e. $(\text{RFF}_1 - \text{RFF}_2)/\text{RFF}_1$, to be larger than 1.0–1.6 (e.g., Hoyos et al. 2012). This is a conservative threshold for the selection of the multi-component fit (RFF_2) to prevent over-fitting. Here, we are more concerned about effectively removing the flux of a given galaxy (to get a smaller residual) rather than provid-

ing a realistic description of its morphology. For this reason we select the multi-component solution when $\text{RFF}_2 < \text{RFF}_1$.

After the modelling process and subtracting both ICL and bright cluster members, we apply a median filter to the cleaned image. This is a well-known smoothing technique that replaces the value of a given pixel by the median of its neighboring pixels (see Merlin et al. 2016a). We use a filter with a box size of 1 deg per

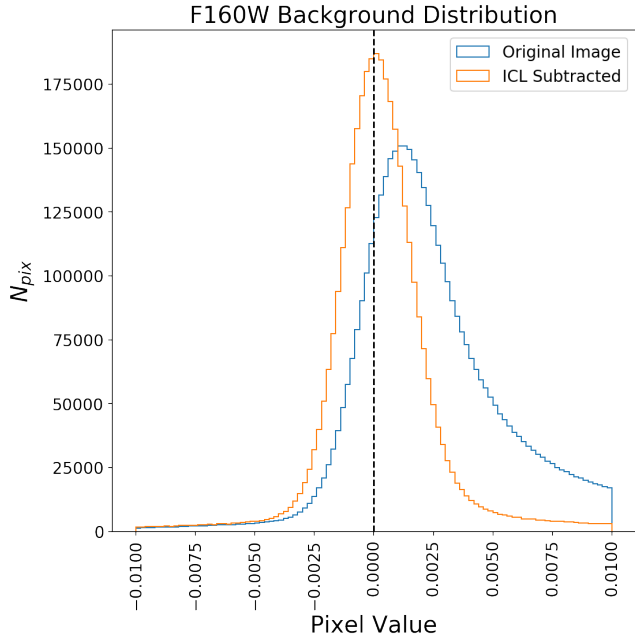


Figure 5. Pixel values of the original background (blue histogram) and after ICL subtraction (orange histogram); the vertical dashed line marks the zero value.

side. We apply this filtering only to pixels with a flux within 1σ of the background level in order to reduce the effects of over-subtraction in the residual. The resulting improvement can be seen in the bottom-right panel of Figure 7. Note that this process does not affect the outskirts of the cluster.

4. SOURCE EXTRACTION

4.1. HST detections

After performing the modelling described in the previous section, we homogenize the various HST bands by matching their respective PSFs. Images in a panchromatic data set, especially if they sample a wide wavelength range like extra-galactic surveys, are usually affected by different PSF shapes (see Figure 3). This means that the fraction of the flux that falls inside an aperture, as well as the resulting noise, varies as a function of bandwidth and pivotal wavelength.

PSF matching is a convolution procedure to solve these problems by reshaping multi-wavelength images into a common reference system having certain resolution and diffraction properties (i.e., the same “target” PSF, see Tomaney & Crotts 1996; Alard & Lupton 1998). It has become a standard technique to measure consistent fluxes over a range of wavelengths (e.g., Galametz et al. 2011) and from different instruments under varied observing conditions (e.g., Laigle et al. 2016a) to effectively characterize the spectral energy distribution (SED) of the observed galaxies.

Specifically, we use the PSF models derived in Section 3.1. In our case, the target PSF is the one in the

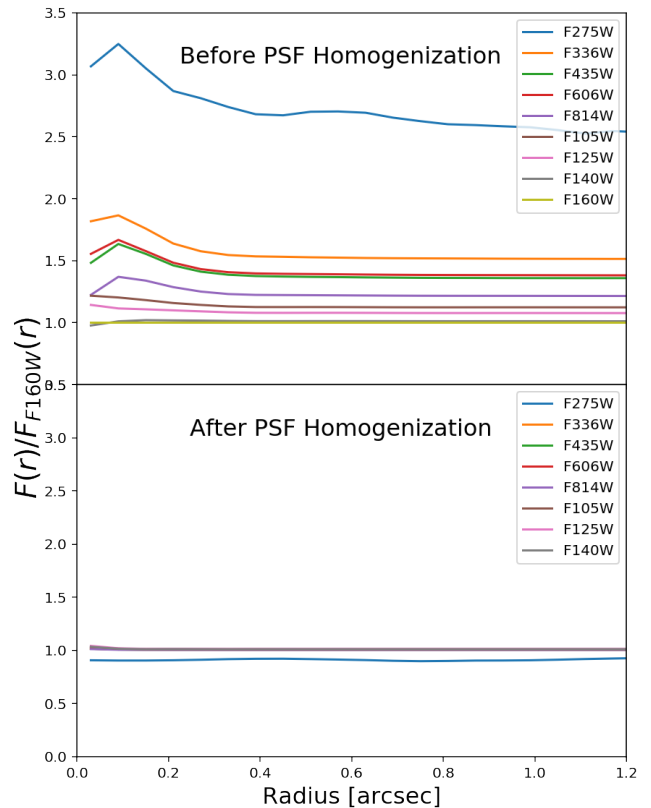


Figure 6. Growth curves for each HST-derived PSF normalized by the F160W growth curve before (top) and after (bottom) homogenization.

F160W band as it is the reddest HST band. To convert the other HST images we use a convolution kernel obtained by taking (in Fourier space) the ratio between their original and target PSFs. Note that in some cases, the target PSF is marginally smaller than the original. Despite this, we are able to relate target and original PSF since we do not require the convolution kernel to be positive-definite. We show the growth curves for the PSFs extracted from the HST data, normalized by the growth curve of the F160W PSF before and after homogenization, in Figure 6. We note that after PSF homogenization, the normalized growth curves are, on average, agree within 2% for all bands except F275W, which agrees at the 8% level. PSF matching is not applied to ground-based images nor *Spitzer*: their resolution is appreciably lower than the HST bands and in that case the photometric extraction is performed with a different method (see Section 4.2).

We then proceed to perform source photometry for each HST image using SE. The strong clustering of the objects in the HFF images pose the additional problem of detection completeness because the objects that are close pairs along the line of sight are not always successfully deblended by the software. To improve the extraction process, we create a co-added IR image from the

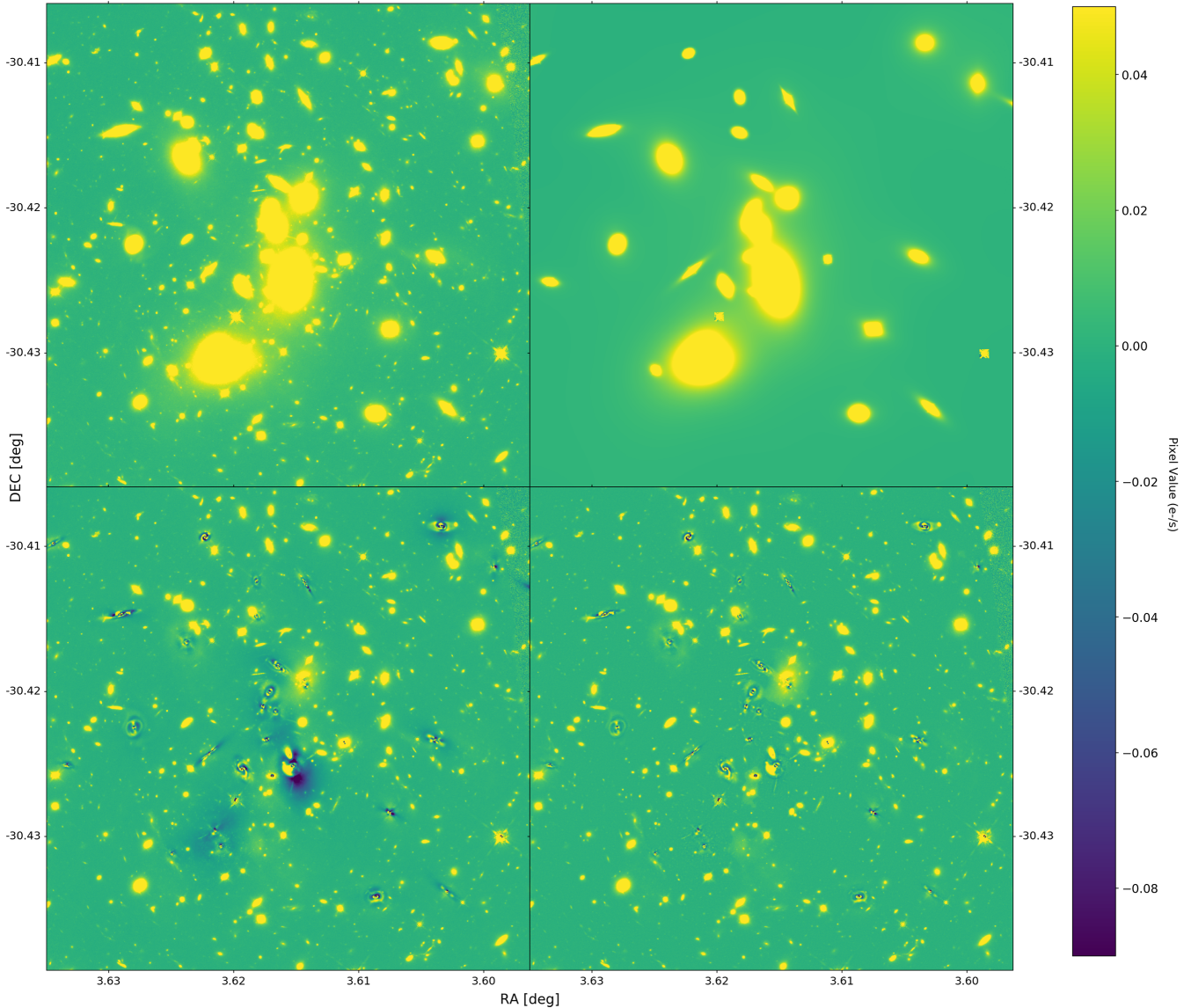


Figure 7. A summary of the various steps in bright cluster + ICL modelling (in this case for cluster Abell 2744). Upper panels show the original image (left) and the galaxy/ICL models (right). Lower panels show the residual image before and after median filtering (left- and right-hand panel respectively). The colorbar denotes the pixel intensity in counts/s. See Sections from 3.2 to 3.3 for more details.

weighted mean, using their inverse variance as weights, of four WFC3 bands (namely F105W, F125W, F140W, and F160W). Such a stacking enhances the signal-to-noise ratio of faint sources, being effectively deeper than any individual band. We use the stack of infrared images as a detection image, running SE in dual mode.

Moreover, given the variety of scientific goals, it is important to precisely measure both the bright galaxies in the foreground and the fainter galaxies in clusters. However, source extraction with SE is a trade-off between rigorous source deblending of galaxies close to each other on the angular plane, and spurious shred-

ding of structure from a single galaxy. For this reason, previous works (Caldwell et al. 2008; Gray et al. 2009; Galametz et al. 2013, and references thereon) proposed a “dual mode”, or High Dynamic Range (HDR), approach with a cold mode and a hot mode SE run, where the cold mode detects and performs photometry on the objects contained within visually reliable Kron radii and the hot mode more aggressively deblends and performs photometry on the smallest and faintest objects. Given the aggressive deblending of the hot mode, it can break up larger objects into individual pieces, which we discard when considering the cold catalog. We modify the

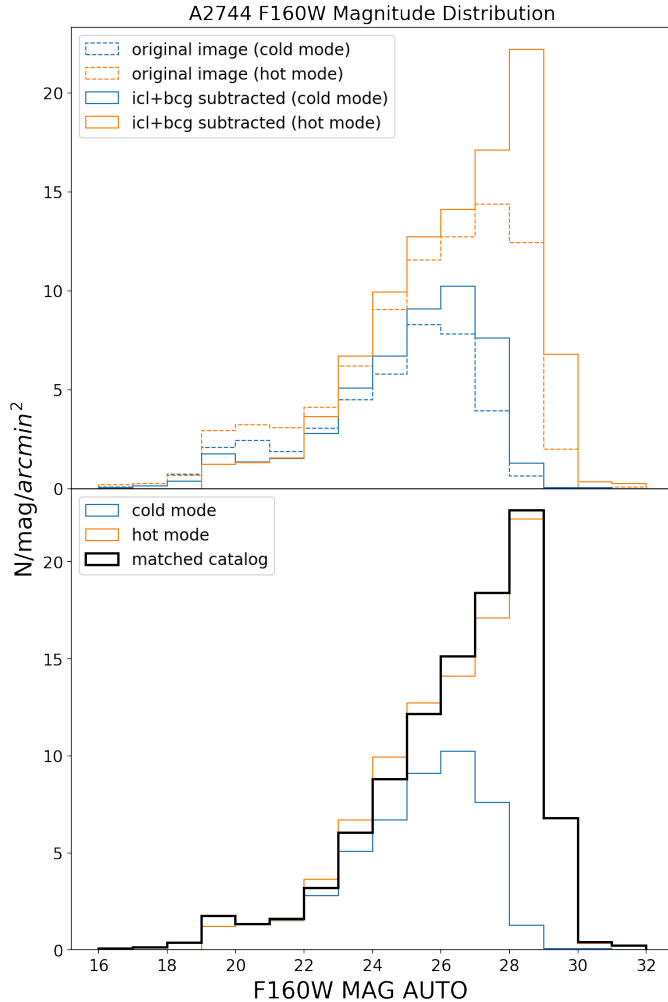


Figure 8. Magnitude distributions for the objects detected using the cold (blue) and hot (orange) modes for the original image v. ICL+BCG subtracted image (top) and ICL+bcg subtracted image (bottom); matched (black) refers to total number of galaxies detected and kept in the catalog per magnitude bin. We see a significant increase in the number of detected galaxies in the cluster subtracted image, as well as a slight shift in mean magnitude toward fainter objects.

HDR approach described in Galametz et al. (2013) and discard galaxies from the hot mode that fall within a $0.2 \times$ Kron radius (Kron 1980) of a cold mode detected object. We show the resulting magnitude distributions of this process in Figure 8.

To alleviate the possibility of fake source detection around the residuals, we utilize the Kron radius of the modeled object and discard objects which fall within it. Furthermore, we remove sources corresponding to diffraction spikes and those susceptible to edge effects on the perimeter of the images. This procedure is performed on both the cluster and parallel fields.

We present the magnitude histograms in the F814W band for each cluster and their parallel fields (Figure 9). It shows the overabundance of bright galaxies in the clusters when compared to the parallel fields. We note that even after ICL+bright galaxy subtraction, the presence of such bright objects diminishes our ability to detect faint objects. We also show the ratio of number counts between the cluster and parallel fields in the F814W and F160W bands (Figure 10). The observed trend here is consistent across all clusters, demonstrating the importance of having parallel fields with comparable depths.

4.2. Photometry in lower resolution images

In addition to HST, we also rely on imaging observations from Keck, VLT, and *Spitzer*. Those facilities have lower angular resolutions than the HST instruments, increasing the blending between sources. In order to maximize the information extracted from each image, we use the prior-based code T-PHOT (Merlin et al. 2016a). This code uses the high-resolution HST images and their corresponding SE catalogs as priors to perform dual-mode photometric extraction in the lower-resolution images. This allows measurement of blended sources that are not directly detectable in K_s or IRAC bands. On the other hand the method misses the so-called “HST dark” sources, i.e. galaxies so faint in optical and near-IR that are not identified in the prior image, even though they are sufficiently bright to be visible in the low-resolution image. HST dark sources may constitute a hidden population of galaxies providing a non-negligible contribution e.g. to the cosmic star formation rate density budget (see Wang et al. 2019). However, the identification of HST dark sources is subsequent to the creation of an HST-based catalog and shall be addressed in future work.

Concerning the *Spitzer* images, before running T-PHOT we perform a series of corrections related to the weight maps (defined as the inverse variance per pixel, i.e. $1/\sigma^2$) using the pull diagnostic (Gross 2018), described as follows. Assuming the distribution is Gaussian, in principle, the ratio between the variable and its standard deviation should produce a Gaussian with a standard deviation (σ) equal to one. In the limit of large statistics (owing to the Central Limit Theorem), we can approximate the signal on the background pixels to follow a Gaussian distribution. For this purpose, we compute the distribution of the ratio between the background level and its standard deviation, σ_{bkg} . Such a distribution is expected to have a standard deviation $\sigma_{\text{pull}} \approx 1$ if σ_{bkg} is properly estimated. A value of $\sigma_{\text{pull}} < 1$ means that the uncertainties are likely underestimated, and $\sigma_{\text{pull}} \gg 1$ means that the uncertainties are likely overestimated. In order to have conservative values for the error maps, we multiply these by σ_{pull} when the latter is greater than one. For *Spitzer* channels 1, 2, 3, and 4 we only correct the error maps in the largest contiguous region where the cluster and parallel fields are located. We check

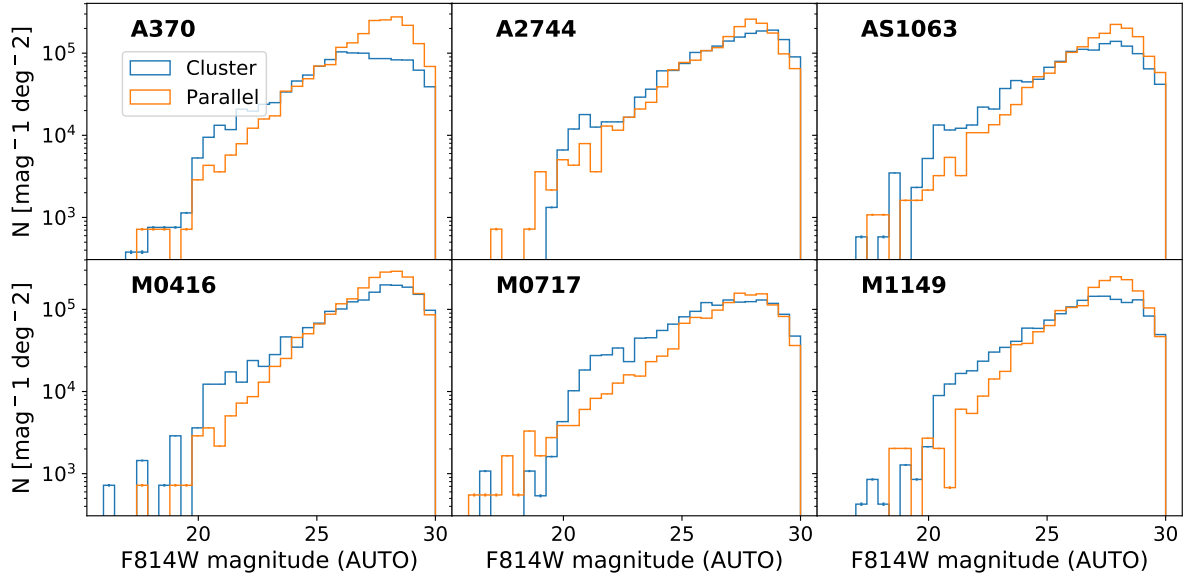


Figure 9. Comparison of magnitude distributions for the HFF cluster and their parallel fields. This clearly shows the excess in number of galaxies in clusters compared to the field. It also shows the field and cluster samples have similar depths.

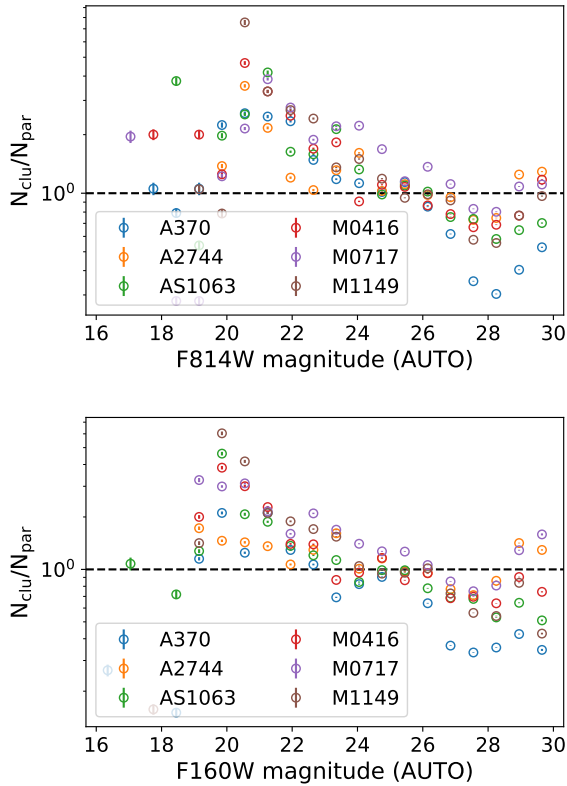


Figure 10. Ratio between magnitude distributions in the parallel and cluster fields for all HFF clusters in the F160W band (top) and F814W band (bottom). The excess of field galaxies over clusters in fainter magnitude bins is likely caused by non-detection of faint sources in clusters due to diffuse light from more luminous objects.

that this is a good approximation since the resulting corrected background distributions show a single peak. The corrected errors, σ_{pull} , are discussed in Appendix A.

As the high resolution prior, we use the science image in the F160W band and the segmentation map created from the weighted IR stack. Previous studies (De Santis et al. 2007; Galametz et al. 2013) found that SE tends to underestimate the isophotal area of objects in a single-band detection image; such a systematic effect is inversely proportional to the flux. A solution to this issue (Galametz et al. 2013; Merlin et al. 2016b) is to dilate the segmentation areas of individual sources. We verify how prominent this effect is by comparing one of the HFF clusters (Abell 370) to the deeper BUFFALO survey, given that the isophotal area increases with increasing signal-to-noise. We choose to compare the HFF IR stack, given its depth, to the BUFFALO F160W band. We find that when using the IR stack the isophotal area of each source is slightly larger, with minimal dependence on the area. The difference is small enough that we found it unnecessary to dilate the segmentation map before feeding it into T-PHOT.

We run T-PHOT for the Ks- and IRAC bands. Because the IRAC PSF varies across the field of view, we take advantage of T-PHOT “multikernel” option, which allows for the inclusion of a separate kernel for each object. These kernels are generated from the grid of PRFs produced by PRFMap, as described in Section 3.1. We emphasize that the output provided by T-PHOT (namely, the parameter FitQty) is an estimate of the *total* flux emitted by the given source.

5. VALIDATION OF THE PHOTOMETRIC CATALOG

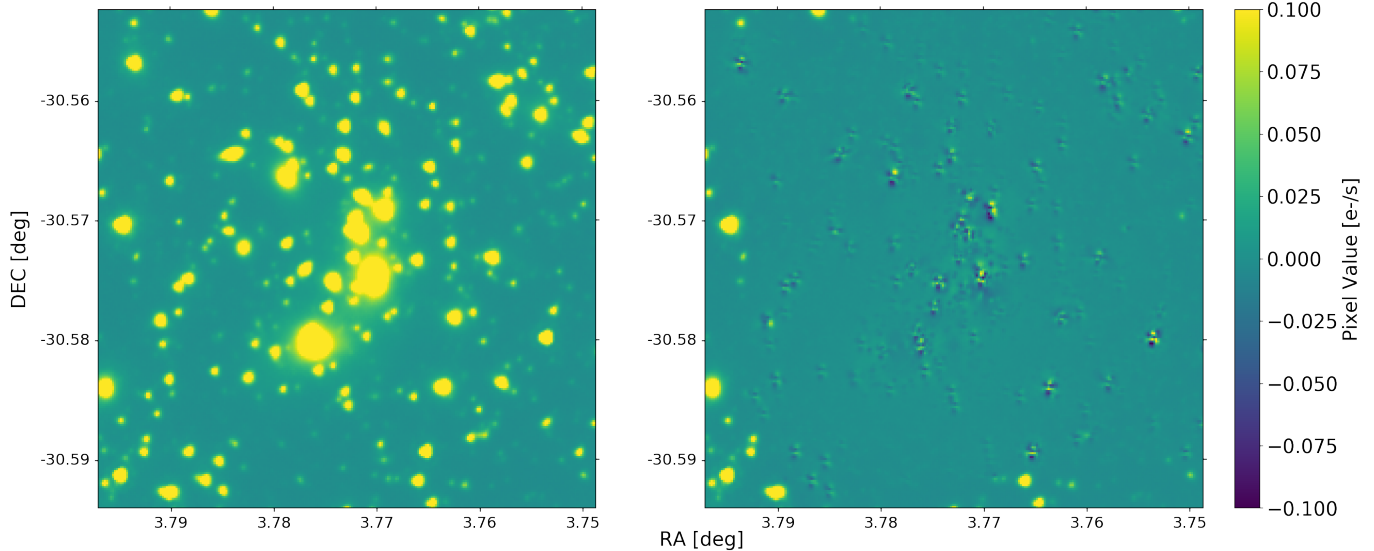


Figure 11. (Left to right) Original IRAC Channel 1 image in Abell 2744 (*left panel*) compared to the residual map (*right panel*) after subtracting T-PHOT galaxy models (see Section 4.2).

5.1. Quality and completeness via simulations

To measure the completeness, we add randomly distributed simulated objects in the observed image and then try to recover them. The number of the simulated objects should be high enough to cover the full field of view and avoid statistical fluctuations, while their surface density should be low enough not to further increase the already large fraction of overlapping sources in the images. This way, we still check the performance of the deblender without introducing an unrealistic number of new blends.

In order to measure completeness we injected 100 point-like sources in the original images, with magnitudes randomly assigned from a uniform distribution between $23 < mag_{AB} < 31$. The magnitudes of these objects were selected to be the same in all bands, which allows us to compute the IR-weighted magnitude straightforwardly. This was done to simplify interpretation of the results. The processing of these images, was performed using the same steps presented in previous sections. We generated two sets of simulations (hereafter called ‘flavors’):

- one set where we assign the position of the injected objects randomly within the image. We will refer to these simulations as flavor 1;
- a set where we assign the centroid position of the injected objects randomly within the empty parts of the image, i.e., where the segmentation map has no detected pixels. We will refer to these simulations as flavor 2.

The reason behind the generation of two sets of simulations is that in the first flavor the fraction of blended objects is overestimated, since we are randomly placing

new sources in a field that is already overcrowded. This leads to a pessimistic characterization of our pipeline’s performance. However, using the second flavor, we explicitly avoid overlap with other sources. In the latter case the quality assessment will be over-optimistic.

Ten independent realizations were generated for each of these flavors, The injected sources were independently generated for each cluster as 15 arcsec-side noise-free square cutouts. We then formed a collage of the same size of the original image, and added this collage to the original image of each cluster. Therefore, only the original noise in the HFF mosaics is affecting the present test. This is a good approximation for faint sources, where the background dominates over the shot noise due to the source itself.

After the injection of simulated sources, these images are analysed by the same software used for the real catalog (see previous Sections). We compare the output to the list of input (simulated) sources, and their intrinsic vs. recovered properties. We considered a source successfully recovered if there is an entry in the output catalogs whose centroid is within 0.6 arcseconds (10 pixels) from the input location, and the offset between intrinsic and extracted magnitude is < 0.5 mag. These thresholds have been chosen to minimize the number of by-chance matches between simulated and real sources, allowing at the same time for some difference between the input and output values.

Results from this test are summarized in Figure 12. For flavor 2 simulations, we find that completeness is above 60% for magnitudes brighter than 29, and above 80% for most of the clusters up to magnitude ~ 28 . This confirms the estimated depth of our images and catalogs. When we do not avoid overlap between the objects (i.e., using flavor 1 simulations) the overall completeness de-

creases noticeably with respect to the simulation where we avoid blending. Thus, we expect the actual completeness of our catalog to be somewhere in between the pessimistic scenario portrayed by our flavor 1 simulations and the optimistic case of our flavor 2 simulations.

5.2. Photometric uncertainties

Given the complexity of the process to detect objects and measure their flux in different bands, an analytic derivation of their associated uncertainties (in flux, position, and other derived quantities) becomes almost intractable. Forward-modeling will enable us to characterize such uncertainties. To this purpose, we inject another set of simulated objects into the original HFF mosaics. This time the simulated sources are realistic galaxy models from the GREAT3 challenge (Miyatake et al. 2014), created by means of `GalSim` (Rowe et al. 2015). `GalSim` is a modular, open-source code to render any type of astronomical images. We opted for the GREAT3 library because it includes models with realistic morphology, obtained by fitting deep COSMOS images with multiple Sérsic profiles (see Mandelbaum et al. 2014, 2015). Given that the galaxies from the GREAT3 challenge available in the `GalSim` catalog only have information for the F140W band, we identify these galaxies in the Laigle et al. (2016b) catalog using their ID values to obtain the magnitudes in the other bands used in our study. In this way we have realistic colors for our injected galaxies across the entire photometric baseline, with the assumption that their morphology does not vary significantly from band to band. We also ensure that the centroid positions are the same across different bands. We convolve each galaxy profile with the corresponding PSF. The 15×15 square arcsec cutout containing the injected objects (and no additional noise) are then added to the original image. We then repeat the photometric extraction process in a similar fashion to what have been done with our data. In particular, we inject 80 objects randomly placed in each image and generate 12 different realizations (images) of those objects in all the HFF bands.

Additionally, we also process the cutouts that only contain the injected objects using the same pipeline; we use the outcomes as “ground truth” to be compared to the catalog resulting from the injection-recovery procedure. To match the two samples we use the same strategy as in Section 5.1. The photometric residuals for each match are then measured. The results are shown in Figures 13 and 14, indicating an unbiased estimate of input magnitudes across different HST bands included in this study ($\langle \text{mag}_{\text{meas}} - \text{mag}_{\text{input}} \rangle < 0.1$ mag), even after ICL subtraction. However, for the IRAC and K bands we find that the recovered objects appear, on average, dimmer than the input. Since the dependence in flux is mild, we decided to include a constant offset to correct for these residuals. In particular, we shift the recovered magnitudes by the median of the residuals found in Fig-

ure 14. These offsets are $\Delta\text{mag} = (0.04, 0.189, 0.195)$ for Ks, IRAC channel 1, and 2, respectively, and are subtracted from the measured magnitude. We explored different possibilities for the origin of this correction including: size of segments in the segmentation map, and the smoothing radius of the ICL profile. However, after modifying these we could not find any significant changes in the initial offsets that we measured. Given their mild dependence on the flux, and the fact that the effect seems to be milder in Ks, where the PSF is closer to that in the HST bands, we concluded that the observed offsets may be a consequence of numerical instabilities at the time of using the PSF kernel that relates the low and high-resolution images. We notice that the injected sources cover different magnitude ranges for different bands, due to the fact that we are injecting galaxies with realistic SEDs from COSMOS. Additionally, we see a different behavior when we compare different bands. In particular, the uncertainties for the recovered fluxes in the F160W band seem to be smaller than in most of the other bands. The reason behind these differences is the larger depth of the images in F160W compared to the other bands. It is particularly interesting to notice larger uncertainties derived for F275W compared to the other HST bands. This is a combination of two factors: first, the SNR for F275W is the lowest of all HST bands; second, this is also the bluest band, where we expect the largest morphological differences with respect to our segmentation map.

We only perform the simulations for the cluster fields. The reason is that we expect these fields to outperform the parallel fields as the later are not affected by the ICL and are less crowded. As a consequence, our measurements for the clusters will set an upper limit for the photometric biases and uncertainties in the parallel fields. As shown in Figure 16, the photometric bias appears to be uncorrelated with position when comparing cluster core offsets with those in the outer regions. Since the source extraction steps in both cluster fields, and parallel fields are the same, the validation tests of the photometric measurements in the cluster fields are also applicable on the parallel fields.

Our forward modeling approach allows us to estimate the accuracy of the flux errors as reported by SE. Using the injected galaxies we compute the forward-modeling estimation of the uncertainty in the flux, which we call δF_{FM} , as the RMS of the difference between the measured flux for the injected sources and the input flux, $\delta F_{\text{FM}} = \sqrt{\langle (F_{\text{meas}} - F_{\text{input}})^2 \rangle}$, where F_{meas} is the measured flux and F_{input} is the injected flux. This estimation is performed in linearly spaced magnitude bins (with a binwidth of 1.6 mag). We then compare δF_{FM} to the mean uncertainties reported by SE in each of the bins, i.e. $\langle \delta F_{\text{SE}} \rangle$. This is done by studying the ratio $r_{\text{corr}} = \frac{\delta F_{\text{FM}}}{\delta F_{\text{SE}}}$ as a function of flux. We fit the resulting ratio to an exponential model $r_{\text{corr}} = AF^b$ and use

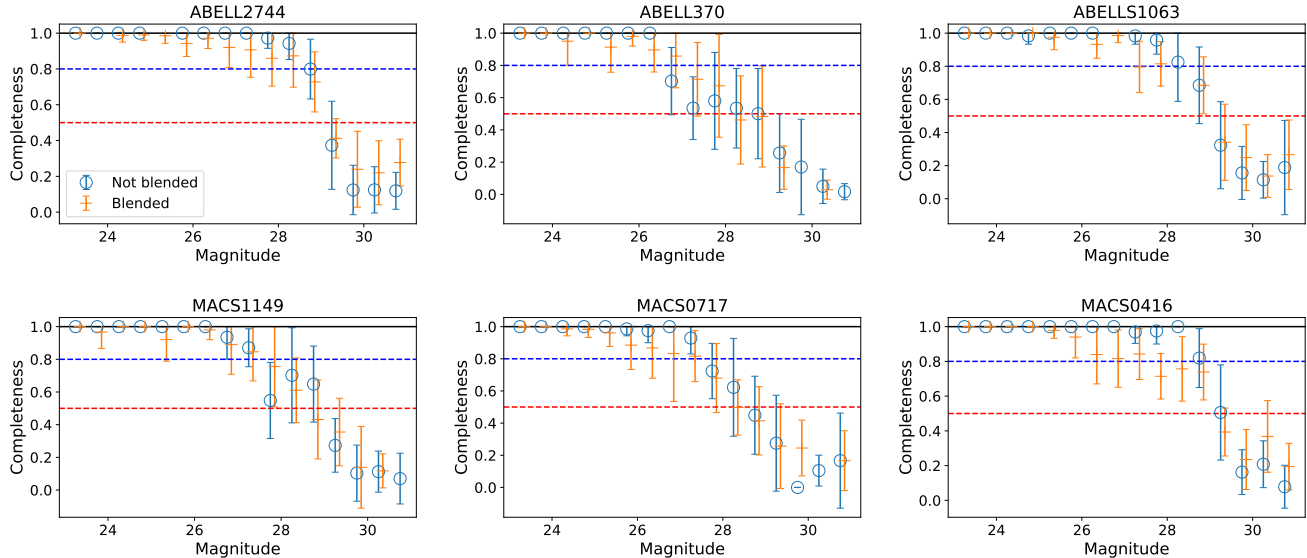


Figure 12. Completeness as a function of magnitude for injected point-like sources between 24 and 30 mag in the six analyzed clusters (*top row*: Abell 2744, Abell 370, Abell S1063; *bottom row*: MACS1149, MACS0717, MACS0416). The positions of these objects were randomly assigned within the footprint (open circles – flavor 1, i.e., not blended) or randomly assigned in empty parts of the segmentation map (crosses – flavor 2). We introduce a small horizontal offset of the different markers and only include the error-bars for the flavor 2 case in order to improve readability. We also add horizontal solid line to mark 100% completeness, and two dashed lines at 80% and 60% completeness as visual help. Detections are made in IR-weighted images.

this fit to correct the reported uncertainties for each detected object. The ratio and resulting fit are shown in Figure 15 for F160W, K_s and IRAC channel 1. The best-fit values for a and b can be found in Table 4. By binning the data we lose information about the effects of blending and correlations between flux uncertainties for individual galaxies, but get a more robust estimation of the overall uncertainty of the ensemble.

5.3. Comparison with previous work

There are other independent studies of the Frontier Fields. Given the complexities of extracting photometry in these deep and crowded fields, it poses a great challenge to determine photometric properties of the objects detected with the desired accuracy. Therefore, we believe there is merit in both exploring the limits of our photometric pipeline and comparing with previous results. Figure 17 shows how our photometry compares with that of the previous teams, ASTRODEEP (Merlin et al. (2016b), Castellano et al. (2016), Di Criscienzo et al. (2017), Bradač et al. (2019)) and DeepSpace (Shiple et al. (2018)) for intersecting bands. For the HST bands, we note that there is general agreement in the photometry between the three methods within 0.05 magnitudes up to $m_{AB} \sim 23$ mag. Beyond this magnitude, our photometry agrees best with the ASTRODEEP team, which could be the result of our reduction procedure being more similar to theirs. Furthermore, we see that the three datasets are statistically compatible up to magnitude ~ 25.5 in most bands. However, in the fainter end, there are statistically significant differences

Table 4. Flux uncertainty correction factors obtained for the different bands used in this work.

Band	a	b
F275W	11.00	0.32
F336W	3.67	0.11
F435W	3.32	0.23
F606W	3.23	0.27
F814W	7.29	0.24
F105W	10.46	0.21
F125W	7.54	0.08
F140W	8.88	0.37
F160W	5.17	0.45
K_s	1.58	0.29
I1	42.31	0.78
I2	46.94	0.71
I3	3.38	0.74
I4	1.09	1.18

between the DeepSpace and ASTRODEEP datasets, and the data presented in this work. These differences are probably due to the difference in modelling, as the

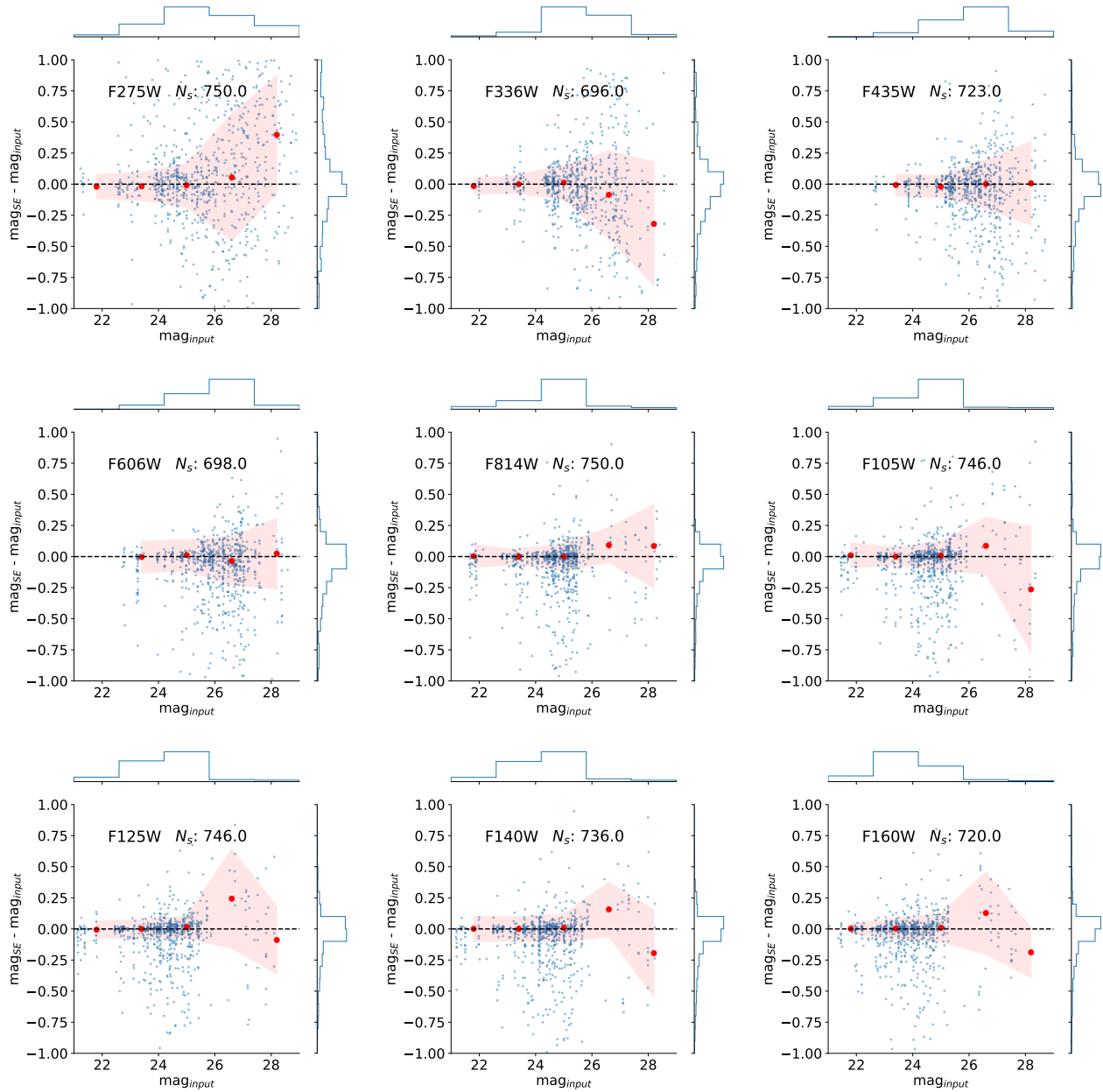


Figure 13. Photometric residuals between the simulated objects injected in the Abell 2744 cluster and the input fluxes, plotted as a function of magnitude for different bands. In each panel, blue small dots are the individual objects residuals, while the red dots represent the median in bins with 1.6 mag width. The shaded region encompasses the rescaled interquartile range, $0.7413(Q3 - Q1)$ as a robust estimator of 1σ uncertainty (Ivezić et al. 2014). The magnitude distribution of each injected sample is projected on the x axis on the top of the corresponding panel, while the photometric residual distribution is shown in the right-hand side of the y axis.

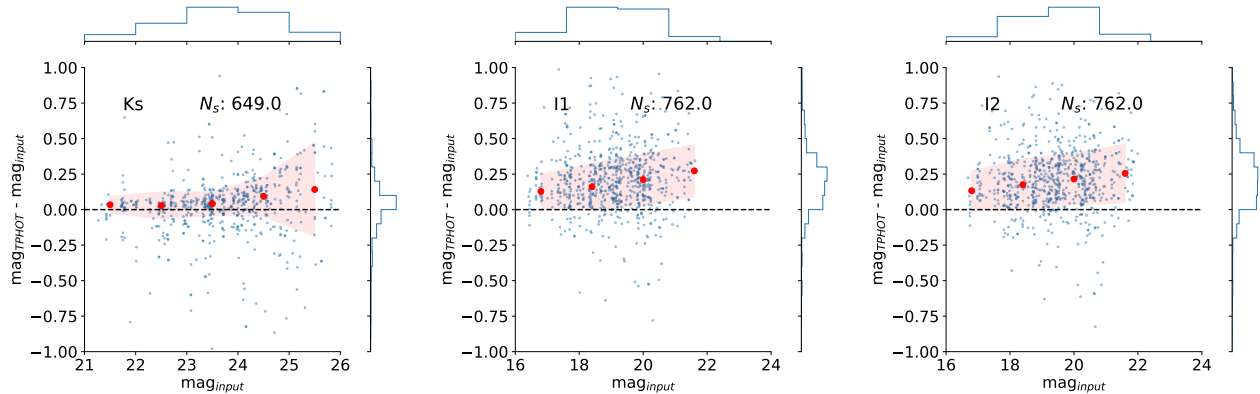


Figure 14. Photometric residuals in ancillary data (K_s band and *Spitzer*/IRAC channels). See the caption of Figure 13 for more details. We find a photometric bias between input and measured magnitude that we correct using the median value of the residual in each band.

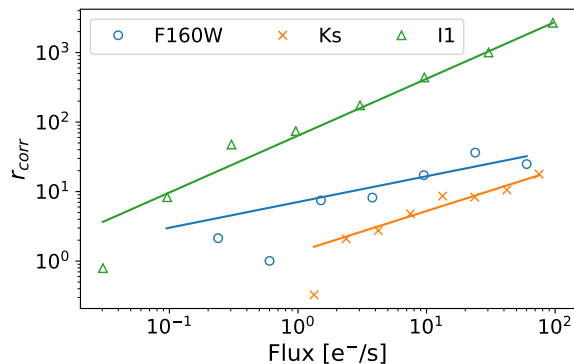


Figure 15. Ratio between the flux uncertainty recovered via forward-modeling and the reported flux uncertainty by Source Extractor in three different bands: F160W (open circles), Ks (\times), and IRAC Channel 1 (open triangles). For each band, a solid line shows the corresponding best-fit model, i.e. the power law $r_{\text{corr}}(F) = aF^b$. The best-fit values found for a and b in the different bands can be found in Table 4.

measure of fluxes/magnitudes depends on the concrete choices for apertures, etc. However, we check that the colors are consistent among these datasets for the HST and Ks bands, which can be inferred by the consistent behavior found in most bands. Thus, for applications where colors are most important (e.g., photometric redshifts) any of these datasets should give similar results (as evidenced by our photometric redshifts).

6. PHOTOMETRIC REDSHIFTS

Having the self-consistent SEDs for individual galaxies in each of the HFF clusters and their associated parallel fields, we now measure the photometric redshifts using LePhare (Arnouts et al. 1999; Ilbert et al. 2006). The code fits galaxy templates to the observed SEDs to derive a redshift likelihood function (\mathcal{L}) for each source. Photometric redshift estimates (z_{phot}) are then defined

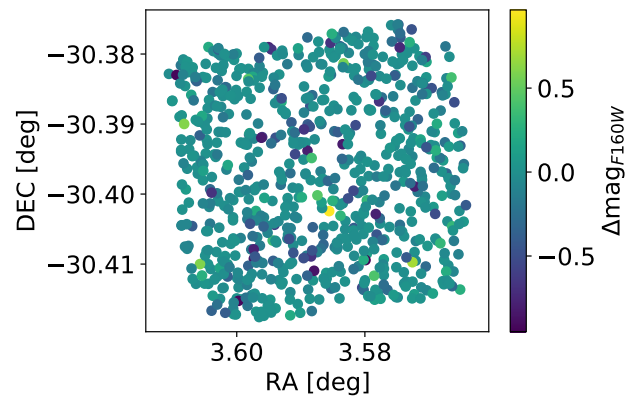


Figure 16. $\Delta\text{mag} = \text{mag}_{\text{output}} - \text{mag}_{\text{input}}$ for the F160W band as a function of the position of detected injected objects for the Abell 2744 cluster. There is no clear correlation between the residual and the position of the injected object in the field. Similar results are observed for the rest of the bands analyzed.

as the median of $\mathcal{L}(z)$. The template library adopted here is the same used in Laigle et al. (2016a) since it was shown that it works efficiently across a wide redshift range (up to $z \sim 6$). The library is built by spiral and elliptical galaxy models from Polletta et al. (2007) along with other ones derived from the stellar population synthesis model of Bruzual & Charlot (2003). The latter is used to reproduce both young quiescent and starburst galaxies. For each model we produce different templates by changing their dust attenuation between $0 < E(B - V) \leq 0.5$ and assuming either Prevot et al. (1984) or Calzetti et al. (2000) extinction laws depending on the galaxy type (see Laigle et al. 2016a for more details). When Calzetti et al. (2000) is chosen, we produce three alternate versions by adding different parametrization of the 2,175 Å bump (see Ilbert et al. 2009). Absorption by the intervening inter-galactic

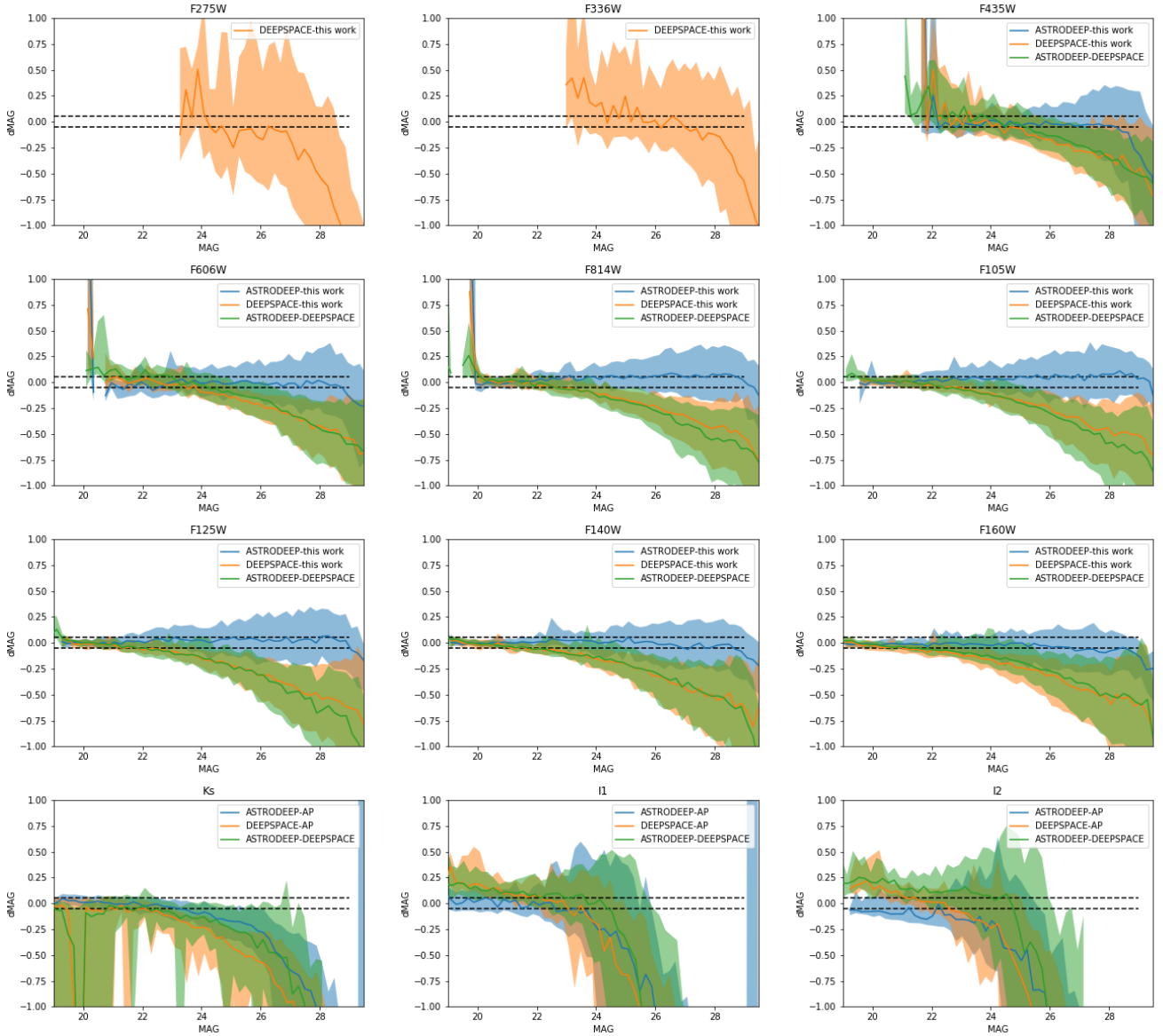


Figure 17. Comparison of our extracted photometry with that of the existing data produced by the ASTRODEEP and DEEPSPACE teams. Shown are the Δmag where data exists for cluster-only photometry in each band. The black dashed lines represent magnitude offsets of ± 0.05 . The solid lines represent the running median and the shaded region represents the interquartile range of those measurements.

medium is also implemented as prescribed in Madau (1995). We also add the main nebular emission lines in rest-frame optical to the templates corresponding to the star-forming SEDs, modelling line fluxes and their ratios as in Saito et al. (2020).

Before running LePhare, a modification is required to the HST bands: the fraction of the flux lost by SE isophotal measurements (FLUX_ISO) must be taken into account. FLUX_ISO provide more accurate colors than FLUX_AUTO, which is another SE photometric measurement specifically designed to recover total flux by means of an adaptive aperture (cf. Kron 1980); therefore the former are preferred for z_{phot} computation. How-

ever, our ancillary photometry is extracted with T-PHOT, which does not provide an equivalent to FLUX_ISO. Therefore, we include in our baseline K_s and IRAC total fluxes while HST bands fluxes are rescaled by a factor

$$f_{\text{tot}} = \frac{\sum_i w_i (\text{FLUX_AUTO}/\text{FLUX_ISO})_i}{\sum_i w_i}, \quad (3)$$

i.e. the weighted mean of the AUTO-to-ISO flux ratio summed over the observed HST bands. Weights are defined as $w = \sqrt{\sigma_{\text{AUTO}}^2 + \sigma_{\text{ISO}}^2}$, i.e. square root of the sum in quadrature of the corresponding SE errors.

In order to empirically correct for systematic effects we perform a calibration that relies on the spectroscopic redshifts (z_{spec}) available in each field. The sample includes spectroscopic data from several programmes retrieved from the NASA/IPAC Extragalactic Database¹¹. The spectroscopic campaigns contributing to the majority of the data set are described in Owers et al. (2011); Ebeling et al. (2014); Richard et al. (2014); Balestra et al. (2016); Treu et al. (2015); Schmidt et al. (2014); Lagattuta et al. (2017); Mahler et al. (2018). We also include more recent observations carried out by Lagattuta et al. (2019) in Abell 370, which were not included in previous photometric redshift analysis in the literature. The calibration procedure is as follows. First, we run **LePhare** on the HFF galaxies with known spectroscopic redshifts after fixing their redshifts to their spectroscopic z_{spec} value. We only consider galaxies with a reliable spectroscopic redshift, i.e. with a “quality flag” >3 .¹² We do not apply any magnitude cut. Once obtained the best-fit solution from **LePhare** (i.e., the fitting model resulting in the smallest χ^2) we measure in each photometric band the difference between the observed flux and the prediction by the best-fit template. To find the systematic offset (in a given band) we compute the average difference in the spectroscopic sample. Since results are similar in the six fields, we eventually consider only the offsets measured for the Abell 370 cluster because it has the largest number of spectroscopic sources (320 of them reliable spectroscopic redshifts). These offsets, when applied to the photometric baseline, will compensate for a possible bias in the template library and/or for calibration issues in data reduction. In the HST bands the corrections are between 2 and 5%, except for the F425W filter which is 8%; a similar value is found for K_s while in the IRAC channels 1 and 2 the correction is a factor 1.11. We note that similar offsets (namely, 0.1 mag in both IRAC channels 1 and 2) have been found by **LePhare** also in another extragalactic survey (Mehta et al. 2018). All offsets are quoted in Table 5, with the exception of IRAC channels 3 and 4 since the systematics here would be mainly driven by the absence of dust re-emission in the templates (see Mehta et al. 2018). To take such a limitation into account we increased the error bars in these two channels by adding 0.5 mag in quadrature, under-weighting in practice their contribution to the fit.

We fit the SED of 1,423 spectroscopic galaxies with $16 < F160W < 26$ across the six clusters to assess z_{phot}

Table 5. Multiplicative factors applied to each band in the photo-z calibration step. The offsets found in the HST bands are consistent with the median magnitude residual values found in Figure 13, showing the robustness of our forward-modelling procedure.

Band	Multiplicative Factor
F275W	1.04
F336W	1.02
F435W	1.07
F606W	0.99
F814W	0.96
F105W	0.98
F125W	1.01
F140W	1.02
F160W	1.01
Ks	1.00
I1	1.11
I2	1.11

quality. The calibration offsets (Table 5) are taken into account. Similar to the previous work (e.g., Brammer et al. 2008), the scatter is defined as the normalized median absolute deviation (NMAD Hoaglin et al. 1983), i.e.

$$\sigma_{\text{NMAD}} = 1.48 \times \text{median} \left(\frac{|\Delta z - \text{median}(\Delta z)|}{1 + z_{\text{spec}}} \right), \quad (4)$$

with $\Delta z \equiv z_{\text{phot}} - z_{\text{spec}}$. The incidence of catastrophic errors η is defined as the fraction of redshift outliers having $|\Delta z| > 0.15(1 + z_{\text{spec}})$. For pathological PDF(z) where the median is not a good approximation of the main peak of the PDF, we used the redshift corresponding to the minimum χ^2 solution (as in (Davidzon et al. 2017)). For the entire sample $\sigma = 0.067$ and $\eta = 10.3\%$ (Figure 18, upper panel). After excluding the outliers we also recompute the mean of Δz to assess the so-called redshift bias (e.g., Masters et al. 2017), which is 0.012 in our case. We repeat the same procedure for the parallel fields, in which a total of only 62 spectroscopic redshifts are available. In that case we estimate $\sigma = 0.044$ with no outliers. Individual cluster field redshift comparisons are shown in Figure 19. In this figure, the comparison is made using the highest quality spectroscopic redshifts. Figure 20 also shows the photometric redshift distribution for objects in each cluster SED fits with a reduced $\chi^2 < 10$.

¹¹ The NASA/IPAC Extragalactic Database (NED) is funded by the National Aeronautics and Space Administration and operated by the California Institute of Technology (<http://ned.ipac.caltech.edu>).

¹² It is common practice that the persons responsible for the z_{spec} measurements assign a quality flag, ranging from 1 to 4, following the scheme proposed for the first time in Le Fèvre et al. (2004), where a flag equal to 4 corresponds to the highest confidence level

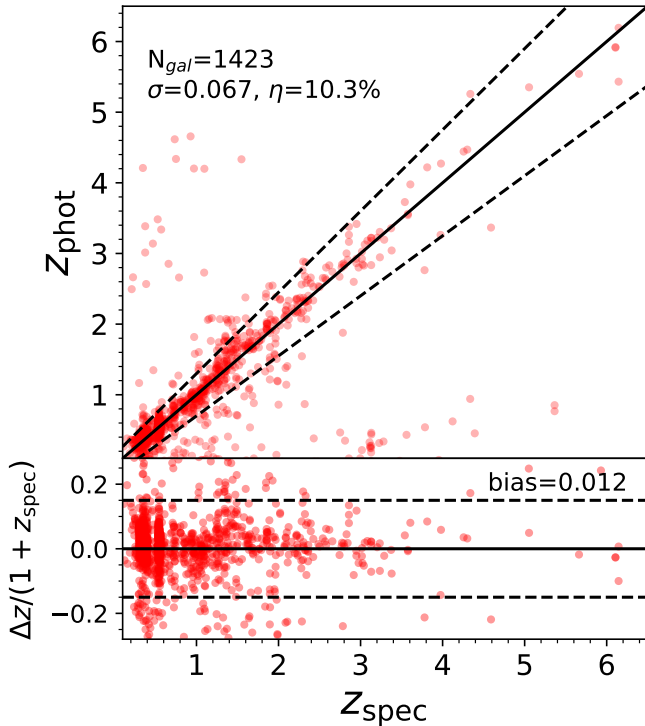


Figure 18. Assessing the quality of photometric redshifts estimated through SED fitting. *Upper panel:* z_{phot} vs. z_{spec} comparison. Red dots are 1,423 spectroscopic redshifts with $16 < F160W < 26$, the solid line shows the 1:1 relationship, and the dashed lines enclose the $z_{\text{phot}} = z_{\text{spec}} \pm 0.15(1 + z_{\text{spec}})$ threshold used to identify outliers (i.e., catastrophic errors). NMAD scatter (σ) and outlier fraction (η) are reported on the top-left corner. *Lower panel:* $\Delta z \equiv z_{\text{phot}} - z_{\text{spec}}$ scatter (red dots are spectroscopic objects) with the median bias indicated by a solid line; dashed lines represent the threshold for catastrophic errors as in the upper panel. See Figure 19 for detailed performance in each individual cluster.

7. DE-MAGNIFICATION

Leveraging the fact that these HFF clusters exhibit some of the strongest lensing currently observed, we calculate and include lens model magnification factors for all relevant objects in our final catalog (i.e. for those objects with redshifts larger than the clusters’ mean redshifts). We use the lens models provided by Bradač (Hoag et al. 2016, and references therein), Caminha (Caminha et al. 2017), CATS (Jauzac et al. 2014, and references therein), DIEGO (Diego et al. 2015, and references therein), GLAFIC (Kawamata et al. 2018, and references therein), Keeton (McCully et al. 2014, and references therein), Merten & Zitrin (Merten et al. 2011, and references therein), Sharon (Jullo et al. 2007; Johnson et al. 2014), and Williams (Jauzac et al. 2014, and references therein) lens modeling teams. We use a script (D. Coe, private comm.) that functions in a

similar way to the Interactive Model Magnification Web Tool¹³ by utilizing the available mass (κ) and shear (γ) maps to directly calculate the magnification factors, and provide the value of the magnification factor, μ , for each lens model in separate columns included in the photometry catalog (see Appendix B for details). Concretely, we compute μ as follows:

$$\mu = \frac{1}{(1 - \kappa)^2 - \gamma^2}. \quad (5)$$

For more information about how these lens models are constructed, we refer the reader to the HFF Lens Modeling webpage¹⁴.

8. DATA PRODUCTS

The final data catalog resulting from this work is accompanied by: (i) the PSF models; (ii) the ICL maps and the bright galaxy models; (iii) median filtered science images with the ICL and galaxy models subtracted; and (iv) photometry, redshift, and magnification catalogs. A brief description of the products is given below:

- i. The PSF models for the HST and Ks bands are released as 2.34x2.34 square arcsecond (39x39 square pixel) fits file arrays. The total flux density of the arrays representing the PSF model is set to unity. IRAC PRFs used in this work are available upon request since they vary across the focal plane.
- ii. The ICL maps and the bright galaxy models are fits arrays of the same resolution and dimensions as the science images. They also use the same units as the science images, that is, ADU/s.
- iii. The ICL+bright galaxy subtracted median filtered images are also fits arrays of the same resolution and dimensions as the science images, in ADU/s units. These are the files on which detection was applied.
- iv. The photometric and redshift catalogs are ascii files for each cluster. For a list of column names, we refer the reader to Appendix B. We also include the photometric offsets used in the photometric redshift calculation in a README file in case the user would like to apply these offsets to the given photometries. Galactic extinction has been applied when calculating photometric redshifts using the $E(B - V)$ values derived from the dust maps presented at Schlafly & Finkbeiner (2011). However, the photometric catalogs do not have galactic extinction applied.

¹³ <https://archive.stsci.edu/prepds/frontier/lensmodels/#magcalc>

¹⁴ <https://archive.stsci.edu/prepds/frontier/lensmodels/>

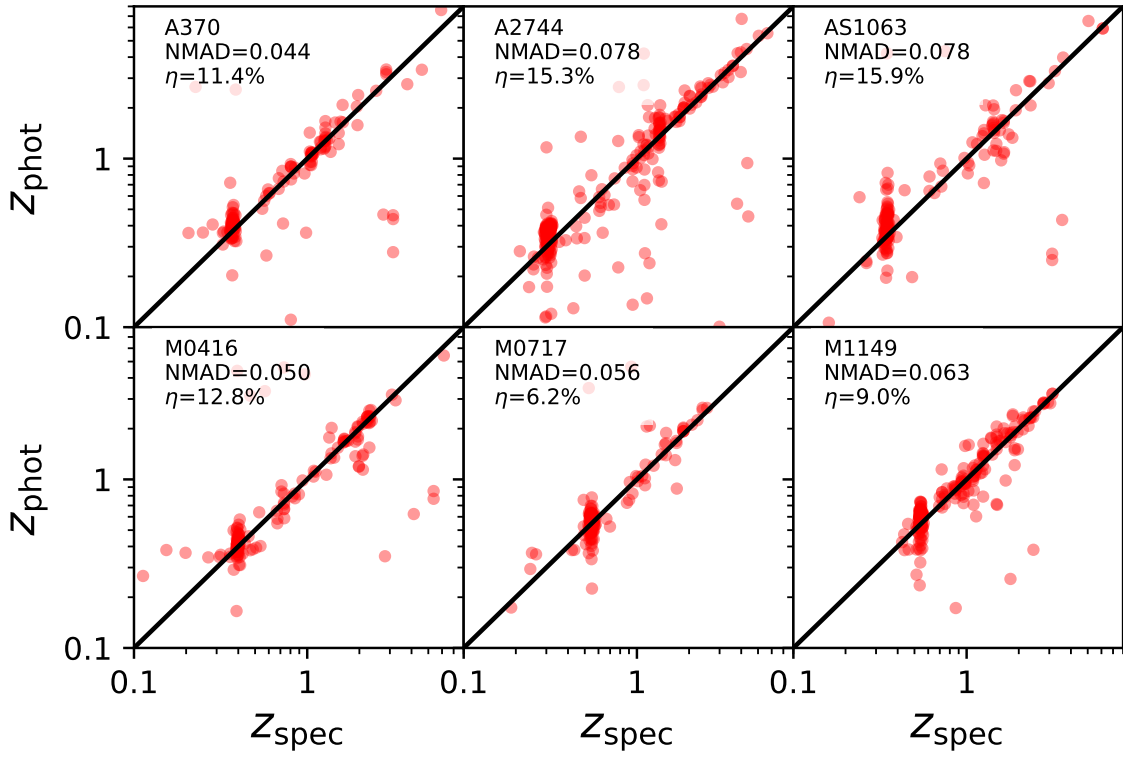


Figure 19. Comparison between z_{phot} and z_{spec} using the most reliable spectroscopic redshift (quality flag equal to 4).

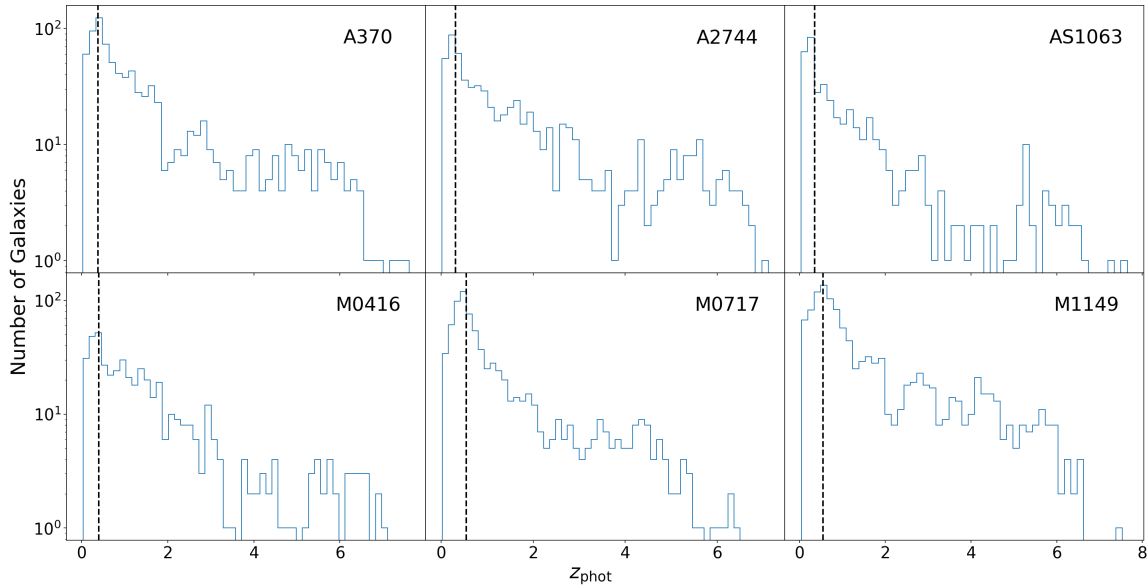


Figure 20. Histogram of the photometric redshift distributions for individual clusters. The black dashed line corresponds to the redshift of the cluster. Objects selected have SED fits with a reduced $\chi^2 < 10$

9. CONCLUSIONS

In this paper we present and publicly release catalogs of the six Frontier Field clusters and their parallel fields. This includes a total of $> 33,500$ objects across a wide wavelength range, $0.275 - 8 \mu m$. We release maps of the intra-cluster light and bright galaxy models. We have outlined the complexity involved in performing this analysis in a crowded field with bright cluster members and intra-cluster light that could bias the measurements. We have successfully removed the contamination from these sources to further reduce the image into a “blank field” on which we can detect the faintest objects in the field without biasing the flux measurements of objects on the perimeter of the field of view. We perform an error analysis using GALSIM by injecting COSMOS-like galaxies to both estimate the errors and to analyse the validity of our pipeline. We note there is no evident photometric bias close to the cluster core as compared to the outskirts.

We estimate the photometric redshifts for objects in all six clusters and their parallel fields as measured by LePhare. When compared to the available spectroscopic redshifts for the HFF clusters, this gives a combined outlier fraction of 10.3% and a redshift bias of 0.012 after excluding the outliers.

We find some differences in our photometry measurements with those from the literature and note the importance of cross-checks between datasets in such crowded and complex environments. We demonstrate the utility of performing source injection, where knowledge of ground truth is accessible to calibrate measurements and characterize biases and uncertainties.

We have scripted a pipeline to analyze each of the Frontier Fields in an efficient, streamlined, and reproducible manner. We plan to apply a similar version of the pipeline to the next generation survey of the Frontier Fields, namely the BUFFALO survey (Steinhardt

et al. 2020) which expands these same fields in area by a factor of 3-4 and pushes the $5-\sigma$ depth ~ 1 magnitude fainter.

ACKNOWLEDGMENTS

The authors would like to thank the anonymous referee for their useful comments and suggestions that improved the overall quality of this manuscript. AP would like to thank A. Alavi, B. Häußler, E. Merlin, and M. Nowinski for useful discussion and comments; AP would also like to thank A. Faisst for providing the code to generate *Spitzer* PRFs that are used in this work. AP acknowledges support from the NASA MUREP Institutional Opportunity (MIRO) through the grant NNX15AP99A. FJS acknowledges that this document was prepared using the resources of the Fermi National Accelerator Laboratory (Fermilab), a U.S. Department of Energy, Office of Science, HEP User Facility. Fermilab is managed by Fermi Research Alliance, LLC (FRA), acting under Contract No. DE-AC02-07CH11359. ID acknowledges the support received from the European Union’s Horizon 2020 research and innovation programme under the Marie Skłodowska-Curie grant agreement No. 896225. This work utilizes gravitational lensing models produced by PIs Bradač, Natarajan & Kneib (CATS), Merten & Zitrin, Sharon, Williams, Keeton, Bernstein and Diego, and the GLAFIC group. This lens modeling was partially funded by the HST Frontier Fields program conducted by STScI. STScI is operated by the Association of Universities for Research in Astronomy, Inc. under NASA contract NAS 5-26555. The lens models were obtained from the Mikulski Archive for Space Telescopes (MAST). This work has made use of the CANDIDE Cluster at the Institut d’Astrophysique de Paris and made possible by grants from the PNCG and the DIM-ACAV. The Cosmic Dawn Center is funded by the Danish National Research Foundation under grant No. 140.

APPENDIX

A. ERROR CORRECTION

In this section we show correction factors applied at various stages in the pipeline. The values for the error map correction from pull-plots calculated in Section 4.2 are shown in Table 6.

B. CATALOG COLUMNS

Each cluster’s photometric catalog has the following columns, with the descriptions taken from each software’s respective documentation (Bertin & Arnouts 1996; Arnouts et al. 1999; Merlin et al. 2016a):

- IDENT: unique galaxy identifier
- ALPHA_J2000: J2000 right ascension of the isophotal image centroid
- DELTA_J2000: J2000 declination of the isophotal image centroid

Table 6. This table contains the correction factors that we apply to Spitzer RMS images for each cluster. The procedure to obtain these correction factors is described in Section 4.2. The different columns refer to different IRAC Channels.

Cluster	$I1$	$I2$	$I3$	$I4$
Abell 370	3.12	2.68	1.03	1.02
MACS J0717.5+3745	2.98	2.74	0.90	0.83
MACS J0416.1-2403	3.04	2.88	0.91	0.86
Abell S1063	2.96	2.73	-	-
Abell 2744	5.83	4.44	0.88	0.85
MACS J1149.5+2223	2.82	2.56	-	-

- FLUX_TOT_BAND: Weighted mean of the AUTO-to-ISO flux ratio
- FLUXERR_TOT_BAND: RMS error estimate for the weighted mean of the AUTO-to-ISO flux ratio
- FLUX_AUTO_BAND: Kron-like automated aperture flux
- FLUXERR_AUTO_BAND: RMS error estimate for Kron-like automated aperture flux
- FLUX_ISO_BAND: Isophotal flux
- FLUXERR_ISO_BAND: RMS error estimate for isophotal flux
- CLASS_STAR: star/galaxy classifier
- FLAGS: source extraction flags
- MAGNIFICATION_{MODEL}: Magnification factors, μ , for each lens map/model. Demagnified fluxes for a given model, MODEL, can be obtained by dividing the preferred flux estimate (e.g., ISO, AUTO) by the value given by MAGNIFICATION_{MODEL}.

There are two photometric redshift catalogs; one where the redshifts were calculated with all bands presented in this work, and one where only HST bands are used. The column order is as follows:

- IDENT: unique galaxy identifier
- Z_BEST: Zphot Best
- Z_BEST68_LOW: Zphot min from $\Delta\chi^2 = 1.0(68\%)$
- Z_BEST68_HIGH: Zphot max from $\Delta\chi^2 = 1.0(68\%)$
- Z_ML: Zphot from Median of ML distribution
- Z_ML68_LOW: Zphot min at 68% of ML distribution
- Z_ML68_HIGH: Zphot max at 68% of ML distribution
- CHI_BEST: lowest galaxy χ^2 for galaxy
- MOD_BEST: galaxy model for best χ^2
- EXTLAW_BEST: Extinction law
- EBV_BEST: E(B-V)
- AGE_BEST: Age (yr)

- PDZ_BEST: Probability per Z bins
- Z_SEC: Galaxy secondary Zphot solution from $F(z)$ function
- CHI_SEC: χ^2 evaluated at secondary Zphot from $F(z)$ function
- MOD_SEC: Galaxy model for CHI_SEC
- EBV_SEC: E(B-V)
- PDZ_SEC: Probability per Z bins for the secondary model
- MOD_STAR: Star solution
- CHI_STAR: χ^2 for star solution
- SCALE_BEST: Scaling factor
- NBAND_USED: Number of bands used for each object
- CONTEXT: Bands to be considered in fit
- ZSPEC: Spectroscopic redshift if available
- MAG_OBS_N: Observed magnitude of band N
- MAG_MOD_N: Predicted model magnitude
- AGE_MED: Age (yr)
- MASS_MED: Rescale Mass (M_{\odot})
- SFR_MED: Rescaled SFR (M_{\odot}/yr)
- ZSPEC_FLAG: Quality flag for Zspec
- ZSPEC_REF: Reference for Zspec
- FIELD: cluster name
- RA: J2000 right ascension of the isophotal image centroid
- DEC: J2000 declination of the isophotal image centroid

REFERENCES

- Alard, C., & Lupton, R. H. 1998, *ApJ*, 503, 325, doi: [10.1086/305984](https://doi.org/10.1086/305984)
- Alavi, A., Siana, B., Richard, J., et al. 2016, *ApJ*, 832, 56, doi: [10.3847/0004-637X/832/1/56](https://doi.org/10.3847/0004-637X/832/1/56)
- Arnouts, S., Cristiani, S., Moscardini, L., et al. 1999, *MNRAS*, 310, 540, doi: [10.1046/j.1365-8711.1999.02978.x](https://doi.org/10.1046/j.1365-8711.1999.02978.x)
- Atek, H., Richard, J., Kneib, J.-P., & Schaerer, D. 2018, *MNRAS*, 479, 5184, doi: [10.1093/mnras/sty1820](https://doi.org/10.1093/mnras/sty1820)
- Balestra, I., Mercurio, A., Sartoris, B., et al. 2016, *ApJS*, 224, 33, doi: [10.3847/0067-0049/224/2/33](https://doi.org/10.3847/0067-0049/224/2/33)
- Barden, M., Häufler, B., Peng, C. Y., McIntosh, D. H., & Guo, Y. 2012, *MNRAS*, 422, 449, doi: [10.1111/j.1365-2966.2012.20619.x](https://doi.org/10.1111/j.1365-2966.2012.20619.x)
- Barkana, R., & Loeb, A. 2001, *PhR*, 349, 125, doi: [10.1016/S0370-1573\(01\)00019-9](https://doi.org/10.1016/S0370-1573(01)00019-9)
- Beckwith, S. V. W., Stiavelli, M., Koekemoer, A. M., et al. 2006, *AJ*, 132, 1729, doi: [10.1086/507302](https://doi.org/10.1086/507302)
- Bertin, E., & Arnouts, S. 1996, *A&AS*, 117, 393, doi: [10.1051/aas:1996164](https://doi.org/10.1051/aas:1996164)
- Bertin, E., & Arnouts, S. 1996, *ApJS*, 117, 393
- Blandford, R., & Narayan, R. 1986, *ApJ*, 310, 568, doi: [10.1086/164709](https://doi.org/10.1086/164709)
- Bradač, M., Huang, K.-H., Fontana, A., et al. 2019, *MNRAS*, 489, 99, doi: [10.1093/mnras/stz2119](https://doi.org/10.1093/mnras/stz2119)
- Brammer, G. B., van Dokkum, P. G., & Coppi, P. 2008, *ApJ*, 686, 1503, doi: [10.1086/591786](https://doi.org/10.1086/591786)

- Brammer, G. B., Marchesini, D., Labbé, I., et al. 2016, *The Astrophysical Journal Supplement Series*, 226, 6, doi: [10.3847/0067-0049/226/1/6](https://doi.org/10.3847/0067-0049/226/1/6)
- Bruzual, G., & Charlot, S. 2003, *MNRAS*, 344, 1000, doi: [10.1046/j.1365-8711.2003.06897.x](https://doi.org/10.1046/j.1365-8711.2003.06897.x)
- Caldwell, J. A. R., McIntosh, D. H., Rix, H.-W., et al. 2008, *ApJS*, 174, 136, doi: [10.1086/521080](https://doi.org/10.1086/521080)
- Calzetti, D., Armus, L., Bohlin, R. C., et al. 2000, *ApJ*, 533, 682
- Caminha, G. B., Grillo, C., Rosati, P., et al. 2017, *A&A*, 600, A90, doi: [10.1051/0004-6361/201629297](https://doi.org/10.1051/0004-6361/201629297)
- Castellano, M., Amorín, R., Merlin, E., et al. 2016, *A&A*, 590, A31, doi: [10.1051/0004-6361/201527514](https://doi.org/10.1051/0004-6361/201527514)
- Davidzon, I., Ilbert, O., Laigle, C., et al. 2017, *A&A*, 605, A70, doi: [10.1051/0004-6361/201730419](https://doi.org/10.1051/0004-6361/201730419)
- De Santis, C., Grazian, A., Fontana, A., & Santini, P. 2007, *NewA*, 12, 271, doi: [10.1016/j.newast.2006.10.004](https://doi.org/10.1016/j.newast.2006.10.004)
- Di Criscienzo, M., Merlin, E., Castellano, M., et al. 2017, *A&A*, 607, A30, doi: [10.1051/0004-6361/201731172](https://doi.org/10.1051/0004-6361/201731172)
- Diego, J. M., Broadhurst, T., Benitez, N., et al. 2015, *MNRAS*, 446, 683, doi: [10.1093/mnras/stu2064](https://doi.org/10.1093/mnras/stu2064)
- Diolaiti, E., Bendinelli, O., Bonaccini, D., et al. 2000, in *Proc. SPIE, Vol. 4007, Adaptive Optical Systems Technology*, ed. P. L. Wizinowich, 879–888
- Ebeling, H., Ma, C.-J., & Barrett, E. 2014, *ApJS*, 211, 21, doi: [10.1088/0067-0049/211/2/21](https://doi.org/10.1088/0067-0049/211/2/21)
- Galamez, A., Grazian, A., Fontana, A., et al. 2013, *ApJS*, 206, 10, doi: [10.1088/0067-0049/206/2/10](https://doi.org/10.1088/0067-0049/206/2/10)
- Galamez, M., Madden, S. C., Galliano, F., et al. 2011, *A&A*, 532, A56, doi: [10.1051/0004-6361/201014904](https://doi.org/10.1051/0004-6361/201014904)
- Gao, L., Springel, V., & White, S. D. M. 2005, *MNRAS*, 363, L66, doi: [10.1111/j.1745-3933.2005.00084.x](https://doi.org/10.1111/j.1745-3933.2005.00084.x)
- Gonzaga, S., & et al. 2012, *The DrizzlePac Handbook*
- Gray, M. E., Wolf, C., Barden, M., et al. 2009, *Monthly Notices of the Royal Astronomical Society*, 393, 1275, doi: [10.1111/j.1365-2966.2008.14259.x](https://doi.org/10.1111/j.1365-2966.2008.14259.x)
- Gross, E. 2018, *CERN Yellow Rep. School Proc.*, 3, 199, doi: [10.23730/CYRSP-2018-003.199](https://doi.org/10.23730/CYRSP-2018-003.199)
- Häufker, B., Bamford, S. P., Vika, M., et al. 2013, *MNRAS*, 430, 330, doi: [10.1093/mnras/sts633](https://doi.org/10.1093/mnras/sts633)
- Hoag, A., Huang, K. H., Treu, T., et al. 2016, *ApJ*, 831, 182, doi: [10.3847/0004-637X/831/2/182](https://doi.org/10.3847/0004-637X/831/2/182)
- Hoaglin, D. C., Mosteller, F., & Tukey, J. W. 1983, *Understanding robust and exploratory data analysis*
- Hoyos, C., Aragón-Salamanca, A., Gray, M. E., et al. 2012, *MNRAS*, 419, 2703, doi: [10.1111/j.1365-2966.2011.19918.x](https://doi.org/10.1111/j.1365-2966.2011.19918.x)
- Ilbert, O., Arnouts, S., McCracken, H. J., et al. 2006, *A&A*, 457, 841
- Ilbert, O., Capak, P., Salvato, M., et al. 2009, *ApJ*, 690, 1236, doi: [10.1088/0004-637X/690/2/1236](https://doi.org/10.1088/0004-637X/690/2/1236)
- Ivezić, Ž., Connolly, A., Vanderplas, J., & Gray, A. 2014, *Statistics, Data Mining and Machine Learning in Astronomy* (Princeton University Press)
- Jauzac, M., Clément, B., Limousin, M., et al. 2014, *MNRAS*, 443, 1549, doi: [10.1093/mnras/stu1355](https://doi.org/10.1093/mnras/stu1355)
- Jauzac, M., Richard, J., Jullo, E., et al. 2015, *MNRAS*, 452, 1437, doi: [10.1093/mnras/stv1402](https://doi.org/10.1093/mnras/stv1402)
- Johnson, T. L., Sharon, K., Bayliss, M. B., et al. 2014, *ApJ*, 797, 48, doi: [10.1088/0004-637X/797/1/48](https://doi.org/10.1088/0004-637X/797/1/48)
- Jullo, E., Kneib, J. P., Limousin, M., et al. 2007, *New Journal of Physics*, 9, 447, doi: [10.1088/1367-2630/9/12/447](https://doi.org/10.1088/1367-2630/9/12/447)
- Kawamata, R., Ishigaki, M., Shimasaku, K., et al. 2018, *ApJ*, 855, 4, doi: [10.3847/1538-4357/aaa6cf](https://doi.org/10.3847/1538-4357/aaa6cf)
- Kneib, J.-P., & Natarajan, P. 2011, *A&A Rv*, 19, 47, doi: [10.1007/s00159-011-0047-3](https://doi.org/10.1007/s00159-011-0047-3)
- Koekemoer, A. M., Faber, S. M., Ferguson, H. C., et al. 2011, *ApJS*, 197, 36
- Kron, R. G. 1980, *ApJS*, 43, 305, doi: [10.1086/190669](https://doi.org/10.1086/190669)
- Kron, R. G. 1980, *ApJS*, 43, 305
- Lagattuta, D. J., Richard, J., Clément, B., et al. 2017, *MNRAS*, 469, 3946, doi: [10.1093/mnras/stx1079](https://doi.org/10.1093/mnras/stx1079)
- Lagattuta, D. J., Richard, J., Bauer, F. E., et al. 2019, *MNRAS*, 485, 3738, doi: [10.1093/mnras/stz620](https://doi.org/10.1093/mnras/stz620)
- Laigle, C., McCracken, H. J., Ilbert, O., et al. 2016a, *ApJS*, 224, 24, doi: [10.3847/0067-0049/224/2/24](https://doi.org/10.3847/0067-0049/224/2/24)
- . 2016b, *ApJS*, 224, 24, doi: [10.3847/0067-0049/224/2/24](https://doi.org/10.3847/0067-0049/224/2/24)
- Laureijs, R., Amiaux, J., Arduini, S., et al. 2011, *arXiv e-prints*, arXiv:1110.3193, <https://arxiv.org/abs/1110.3193>
- Le Fèvre, O., Vettolani, G., Paltani, S., et al. 2004, *A&A*, 428, 1043, doi: [10.1051/0004-6361:20048072](https://doi.org/10.1051/0004-6361:20048072)
- Lotz, J. M., Koekemoer, A., Coe, D., et al. 2017, *ApJ*, 837, 97, doi: [10.3847/1538-4357/837/1/97](https://doi.org/10.3847/1538-4357/837/1/97)
- Madau, P. 1995, *ApJ*, 441, 18, doi: [10.1086/175332](https://doi.org/10.1086/175332)
- Mahler, G., Richard, J., Clément, B., et al. 2018, *MNRAS*, 473, 663, doi: [10.1093/mnras/stx1971](https://doi.org/10.1093/mnras/stx1971)
- Mandelbaum, R., Rowe, B., Bosch, J., et al. 2014, *ApJS*, 212, 5, doi: [10.1088/0067-0049/212/1/5](https://doi.org/10.1088/0067-0049/212/1/5)
- Mandelbaum, R., Rowe, B., Armstrong, R., et al. 2015, *MNRAS*, 450, 2963, doi: [10.1093/mnras/stv781](https://doi.org/10.1093/mnras/stv781)
- Masters, D. C., Stern, D. K., Cohen, J. G., et al. 2017, *ApJ*, 841, 111, doi: [10.3847/1538-4357/aa6f08](https://doi.org/10.3847/1538-4357/aa6f08)
- McCully, C., Keeton, C. R., Wong, K. C., & Zabludoff, A. I. 2014, *MNRAS*, 443, 3631, doi: [10.1093/mnras/stu1316](https://doi.org/10.1093/mnras/stu1316)
- McLeod, D. J., McLure, R. J., & Dunlop, J. S. 2016, *MNRAS*, 459, 3812, doi: [10.1093/mnras/stw904](https://doi.org/10.1093/mnras/stw904)

- Mehta, V., Scarlata, C., Capak, P., et al. 2018, *ApJS*, 235, 36, doi: [10.3847/1538-4365/aab60c](https://doi.org/10.3847/1538-4365/aab60c)
- Merlin, E., Bourne, N., Castellano, M., et al. 2016a, *A&A*, 595, A97, doi: [10.1051/0004-6361/201628751](https://doi.org/10.1051/0004-6361/201628751)
- Merlin, E., Amorín, R., Castellano, M., et al. 2016b, *A&A*, 590, A30, doi: [10.1051/0004-6361/201527513](https://doi.org/10.1051/0004-6361/201527513)
- Merten, J., Coe, D., Dupke, R., et al. 2011, *MNRAS*, 417, 333, doi: [10.1111/j.1365-2966.2011.19266.x](https://doi.org/10.1111/j.1365-2966.2011.19266.x)
- Miralda-Escudé, J. 2003, *Science*, 300, 1904, doi: [10.1126/science.1085325](https://doi.org/10.1126/science.1085325)
- Miyatake, H., Mandelbaum, R., & Rowe, B. 2014, *Journal of Instrumentation*, 9, C04031, doi: [10.1088/1748-0221/9/04/C04031](https://doi.org/10.1088/1748-0221/9/04/C04031)
- Montes, M., & Trujillo, I. 2019, *MNRAS*, 482, 2838, doi: [10.1093/mnras/sty2858](https://doi.org/10.1093/mnras/sty2858)
- Morishita, T., Abramson, L. E., Treu, T., et al. 2017, *ApJ*, 846, 139, doi: [10.3847/1538-4357/aa8403](https://doi.org/10.3847/1538-4357/aa8403)
- Owers, M. S., Randall, S. W., Nulsen, P. E. J., et al. 2011, *ApJ*, 728, 27, doi: [10.1088/0004-637X/728/1/27](https://doi.org/10.1088/0004-637X/728/1/27)
- Paranjape, A., Hahn, O., & Sheth, R. K. 2018, *MNRAS*, 476, 3631, doi: [10.1093/mnras/sty496](https://doi.org/10.1093/mnras/sty496)
- Peng, C. Y., Ho, L. C., Impey, C. D., & Rix, H.-W. 2010, *AJ*, 139, 2097, doi: [10.1088/0004-6256/139/6/2097](https://doi.org/10.1088/0004-6256/139/6/2097)
- Polletta, M., Tajer, M., Maraschi, L., et al. 2007, *ApJ*, 663, 81
- Postman, M., Coe, D., Benítez, N., et al. 2012, *ApJS*, 199, 25, doi: [10.1088/0067-0049/199/2/25](https://doi.org/10.1088/0067-0049/199/2/25)
- Prevot, M. L., Lequeux, J., Prevot, L., Maurice, E., & Rocca-Volmerange, B. 1984, *Astronomy and Astrophysics* (ISSN 0004-6361), 132, 389
- Richard, J., Jauzac, M., Limousin, M., et al. 2014, *MNRAS*, 444, 268, doi: [10.1093/mnras/stu1395](https://doi.org/10.1093/mnras/stu1395)
- Rix, H.-W., Barden, M., Beckwith, S. V. W., et al. 2004, *ApJS*, 152, 163, doi: [10.1086/420885](https://doi.org/10.1086/420885)
- Rowe, B. T. P., Jarvis, M., Mandelbaum, R., et al. 2015, *Astronomy and Computing*, 10, 121, doi: [10.1016/j.ascom.2015.02.002](https://doi.org/10.1016/j.ascom.2015.02.002)
- Saito, S., de la Torre, S., Ilbert, O., et al. 2020, *MNRAS*, 494, 199, doi: [10.1093/mnras/staa727](https://doi.org/10.1093/mnras/staa727)
- Sampaio-Santos, H., Zhang, Y., Ogando, R. L. C., et al. 2020, arXiv e-prints, arXiv:2005.12275, <https://arxiv.org/abs/2005.12275>
- Schlafly, E. F., & Finkbeiner, D. P. 2011, *ApJ*, 737, 103, doi: [10.1088/0004-637X/737/2/103](https://doi.org/10.1088/0004-637X/737/2/103)
- Schmidt, K. B., Treu, T., Brammer, G. B., et al. 2014, *ApJL*, 782, L36, doi: [10.1088/2041-8205/782/2/L36](https://doi.org/10.1088/2041-8205/782/2/L36)
- Schneider, P. 1984, *A&A*, 140, 119
- Scoville, N., Aussel, H., Brusa, M., et al. 2007, *ApJS*, 172, 1
- Shiple, H. V., Lange-Vagle, D., Marchesini, D., et al. 2018, *ApJS*, 235, 14, doi: [10.3847/1538-4365/aaacce](https://doi.org/10.3847/1538-4365/aaacce)
- Spergel, D., Gehrels, N., Baltay, C., et al. 2015, arXiv e-prints, arXiv:1503.03757, <https://arxiv.org/abs/1503.03757>
- Steinhardt, C. L., Jauzac, M., Acebron, A., et al. 2020, *ApJS*, 247, 64, doi: [10.3847/1538-4365/ab75ed](https://doi.org/10.3847/1538-4365/ab75ed)
- Tomaney, A. B., & Crotts, A. P. S. 1996, *AJ*, 112, 2872, doi: [10.1086/118228](https://doi.org/10.1086/118228)
- Treu, T., Schmidt, K. B., Brammer, G. B., et al. 2015, *ApJ*, 812, 114, doi: [10.1088/0004-637X/812/2/114](https://doi.org/10.1088/0004-637X/812/2/114)
- Wang, T., Schreiber, C., Elbaz, D., et al. 2019, *Nature*, 572, 211, doi: [10.1038/s41586-019-1452-4](https://doi.org/10.1038/s41586-019-1452-4)
- Williams, R. 1995, *The Hubble Deep Field*, HST Proposal